Annals of Physics 356 (2015) 57–82

Contents lists available at ScienceDirect

Annals of Physics

journal homepage: www.elsevier.com/locate/aop

Excited-state quantum phase transitions in systems with two degrees of freedom: II. Finite-size effects

Pavel Stránský [a], Michal Macek [a,b], Amiram Leviatan [c], Pavel Cejnar [a,*]

[a] Institute of Particle and Nuclear Physics, Faculty of Mathematics and Physics, Charles University, V Holešovičkách 2, 18000 Prague, Czech Republic

[b] Center for Theoretical Physics, Sloane Physics Laboratory, Yale University, New Haven, CT 06520-8120, USA

[c] Racah Institute of Physics, The Hebrew University, 91904 Jerusalem, Israel

HIGHLIGHTS

- Oscillatory components of state density and spectral flow studied near ESQPTs.
- Enhanced finite-size precursors of ESQPT caused by fully/partly separable dynamics.
- These precursors appear due to criticality of a subsystem with lower dimension.
- Separability-induced finite-size effects disappear in case of fully chaotic dynamics.

ARTICLE INFO

Article history:
Received 1 August 2014
Accepted 16 February 2015
Available online 25 February 2015

Keywords:
Quantum phase transitions
Finite-size effects
Oscillatory component of level density
Regular/chaotic dynamics

ABSTRACT

This article extends our previous analysis Stránský et al. (2014) of Excited-State Quantum Phase Transitions (ESQPTs) in systems of dimension two. We focus on the oscillatory component of the quantum state density in connection with ESQPT structures accompanying a first-order ground-state transition. It is shown that a separable (integrable) system can develop rather strong finite-size precursors of ESQPT expressed as singularities in the oscillatory component of the state density. The singularities originate in effectively 1-dimensional dynamics and in some cases appear in multiple replicas with increasing excitation energy. Using a specific model example, we demonstrate that these precursors are rather resistant to proliferation of chaotic dynamics.

* Corresponding author.
E-mail address: pavel.cejnar@mff.cuni.cz (P. Cejnar).

http://dx.doi.org/10.1016/j.aop.2015.02.025
0003-4916/

1. Introduction

This paper is a continuation of the systematic analysis of Excited-State Quantum Phase Transitions (ESQPTs) in systems with a low number of degrees of freedom f, particularly $f = 2$. The analysis was initiated in Ref. [1], further referred as part I, which investigated the asymptotic-size properties of various types of ESQPT and their dependence on f. In the present part II of our analysis, we focus on some *finite-size precursors* of ESQPTs and their relation to the regular/chaotic nature of the system's dynamics.

Excited-state quantum phase transitions represent a generalization of the ground-state quantum phase transitions to the excited domain. The concept was introduced in Refs. [2–4] as a singularity in the spectrum of quantized energy levels of the system. The singularity affects simultaneously the level density (as a function of excitation energy) and the level dynamics (as a function of system's control parameters), both in a way that strongly depends on the number f of freedom degrees. The ESQPT also leads to various dynamical and thermodynamical consequences, which at present are only partially explored, and has a potential impact on the techniques of quantum information processing. A list of some ESQPT-related papers can be found in part I. The most recent achievements in this field include Ref. [5], which presents an analysis of ESQPTs in molecular systems and a comparison with relevant experimental data, Ref. [6], reporting on the ESQPT observation in microwave Dirac billiards that simulate electronic properties of graphene, and Refs. [7,8], where the ESQPT is investigated in the atom–field quantum optical systems.

The ESQPT concept is usually applied in systems with an asymptotically increasing size, $\aleph \to \infty$, but with a finite (usually small) number of degrees of freedom, $f = \text{const}$. One typically deals with some collective degrees of freedom of a many-body system that consists of a growing number of elementary constituents. The ESQPTs in such systems are associated with various types of *stationary points* of the classical Hamiltonian, which produce some singularities in the spectra of quantum energies for large values of $\aleph$. The reason for the finite-f requirement is the fact that in an infinite-dimensional configuration space any stationary point having a conceivable impact on the quantum state density would have to be "infinitely flat" [9]. Therefore, dealing with ordinary types of stationary points, we need to keep the configuration-space dimension finite. This makes it possible to develop a consistent description and even a classification of ESQPT phenomena in terms of the underlying type of stationary point in the given dimension f.

The finite-f assumption has one crucial consequence. As a rule, the size parameter for systems with a finite number of freedom degrees turns out to be inversely proportional to the Planck constant, $\aleph \propto \hbar^{-1}$. This is so for algebraic systems, for which f is associated with the rank of the dynamical algebra while $\aleph$ coincides with the number of sites or constituents on which the algebra is realized, as well as for non-algebraic systems, where the relation must be elaborated from the scaling arguments [1]. This implies that in the $\aleph \to \infty$ limit, in which the ESQPT singularities would become truly nonanalytic, the system becomes classical. We have to infer, therefore, that quantum critical phenomena in finite-f systems can be observed only in the form of precursors in the spectra for some finite values of $\aleph$. Hence the notion of "*quantum phase transitions in finite systems*".

As discussed in part I of this work, the ESQPT can be defined and classified via the smooth component of the total quantum state density. The smooth component is determined by the phase space integral measuring the $(2f-1)$-dimensional volume of the energy hypersurface in the $2f$-dimensional phase space. We have shown, for Hamiltonians with a quadratic kinetic term and an analytic potential, that nonanalyticity of the smoothed state density is always associated with a stationary point of the potential. We have provided a classification of such nonanalyticities in terms of the corresponding type of stationary point. We have also shown that the nonanalyticity in the state density is reflected by some singular properties of the "flow" of the spectrum as a function of the control parameter and by some anomalies in the system's thermodynamical features.

In the present part II, we focus on the behavior of the *oscillatory component* of the quantum state density in presence of ESQPT singularities of various types. Although the oscillatory component represents just a *finite-size* attribute of the system (in the infinite system the oscillatory component is "averaged out"), we will demonstrate that it may generate essential precursors of the ESQPT—precursors that in a finite system may be even more noticeable than the signatures derived from the smooth

component of the state density. Moreover, it will be shown that the ESQPT effects related to the oscillatory component depend significantly on whether the system exhibits fully regular, fully chaotic, or transitional classical dynamics.

The plan of this article is as follows: Section 2 introduces the oscillatory component of the state density and outlines its impact on the level dynamics and thermodynamic properties of the system. In Section 3, we fix the Hamiltonian of the 2D test model and describe its basic features with respect to the order/chaos competition. Section 4 will be focused on a fully integrable version of the Hamiltonian, in which the x and y degrees of freedom are mutually separated. We will see that separability of the problem leads to significant finite-size precursors of ESQPTs in the oscillatory component of the state density. Section 5 will be devoted to finite-size ESQPT effects for partially or fully chaotic Hamiltonians, illustrating some peculiar ways how the above precursors may partly survive even with an increasing degree of chaos. Section 6 will bring a short summary and outlook.

2. Oscillatory component of state density

Before addressing specific, model-dependent examples of finite-size ESQPT precursors, we present some general considerations on the oscillatory state density. At first we provide some basic definitions (Section 2.1), then we deduce an influence of the oscillatory state density on the level dynamics and thermodynamic properties of the system (Section 2.2), and finally we briefly review the periodic-orbit approximation (Section 2.3).

2.1. Basic expressions

Using the decomposition $\rho^\lambda(E) = \bar{\rho}^\lambda(E) + \widetilde{\rho}^\lambda(E)$ of the total state density $\rho^\lambda(E)$ into the smooth and oscillatory components $\bar{\rho}^\lambda(E)$ and $\widetilde{\rho}^\lambda(E)$, respectively, and invoking the phase-space integral formula for the smooth component, one immediately gets an exact (but trivial) expression of the oscillatory component:

$$\widetilde{\rho}^\lambda(E) = \underbrace{\sum_i \delta(E - E_i^\lambda)}_{\rho^\lambda(E)} - \underbrace{\left(\frac{\aleph}{2\pi}\right)^f \int \cdots \int d^f\vec{p}\, d^f\vec{x}\ \delta\big[E - H^\lambda(\vec{p},\vec{x})\big]}_{\bar{\rho}^\lambda(E)}, \tag{1}$$

where λ is a control parameter of the system and H^λ its classical Hamiltonian. From the practical viewpoint, it may be more convenient to use a partially smoothed, thus *regularized form* of this equation:

$$\widetilde{\rho}_\sigma^\lambda(E) = \underbrace{\sum_i \delta_\sigma(E - E_i^\lambda)}_{\rho_\sigma^\lambda(E)} - \bar{\rho}^\lambda(E), \tag{2}$$

where $\delta_\sigma(E)$ represents a sharp but smooth spike function, which replaces the δ-function from Eq. (1). For instance, one can employ a Gaussian form $\delta_\sigma(E) = \exp(-E^2/2\sigma^2)/\sqrt{2\pi\sigma^2}$ of width σ that roughly coincides with the spacing $\Delta E_i^\lambda = E_{i+1}^\lambda - E_i^\lambda$ between neighboring energy levels of the system.

It is clear that in the infinite-size limit, $\aleph \to \infty$ (equivalent to $\hbar \to 0$), the exact state density $\rho^\lambda(E)$ becomes an infinitely dense chain of δ-functions. An arbitrary smoothening of this function over an infinitely narrow energy interval around E (e.g., using Gaussian of an infinitesimal width σ) yields precisely the value $\bar{\rho}^\lambda(E)$ of the smooth component (determined by the phase-space integral). In this sense, i.e., assuming an infinitesimal ($\sigma \to 0$) smoothing procedure, one can infer that $\widetilde{\rho}_\sigma^\lambda(E) \equiv \widetilde{\rho}^\lambda(E)$ tends to zero as $\aleph \to \infty$. Therefore, analyzing the oscillatory component of the state density, we deal only with finite-size effects.

Note that in analogy to the $\rho^\lambda(E) \leftrightarrow \rho_\sigma^\lambda(E)$ replacement of the total state density in Eq. (2), it sometimes turns relevant to apply a similar replacement also to the smooth component: $\bar{\rho}^\lambda(E) \leftrightarrow \bar{\rho}_\Sigma^\lambda(E) = \sum_i \delta_\Sigma(E - E_i^\lambda)$. Here we naturally assume a smoothing width Σ much larger than the width σ considered above, hence $\Sigma \gg \sigma \sim \Delta E_i^\lambda$.

2.2. Impact on level dynamics and thermodynamic properties

The regularized expressions of the state density (defined in the previous subsection) enable us to quantify the effects of the oscillatory state density on the level dynamics and thermodynamic properties. Following the considerations described in Section 2.5 of part I [1], we characterize the variation of the system's spectrum induced by a change of control parameter λ through the so-called flow rate. In part I, we defined this quantity only via its smooth component. Here – in a full analogy to the level density case – we introduce also the oscillatory and total flow rates:

$$\phi^\lambda(E) \leftrightarrow \phi^\lambda_\sigma(E) \equiv \frac{1}{\rho^\lambda_\sigma(E)} \sum_i \delta_\sigma(E - E^\lambda_i) \frac{dE^\lambda_i}{d\lambda} \quad \text{total flow rate,} \tag{3}$$

$$\bar{\phi}^\lambda(E) \leftrightarrow \bar{\phi}^\lambda_\Sigma(E) \equiv \frac{1}{\bar{\rho}^\lambda_\Sigma(E)} \sum_i \delta_\Sigma(E - E^\lambda_i) \frac{dE^\lambda_i}{d\lambda} \quad \text{smoothed flow rate,} \tag{4}$$

$$\widetilde{\phi}^\lambda(E) \leftrightarrow \widetilde{\phi}^\lambda_\sigma(E) \equiv \phi^\lambda_\sigma(E) - \bar{\phi}^\lambda_\Sigma(E) \quad \text{oscillatory flow rate.} \tag{5}$$

The sums in the first two lines represent Gaussian-weighted averages of the λ-derivatives of individual level energies across $\sigma \ll \Sigma$ intervals around energy E. Prefactors in both these expressions assure normalization of sums of the respective weights to unity. The present notation differs from part I, where we used symbol σ in relation to the smoothed flow rate.

The flow rate quantities introduced above represent essential characteristics of level dynamics for a general system. While the smoothed flow rate $\bar{\phi}^\lambda_\Sigma(E)$ determines an average local slope of the spectrum with parameter λ at energy E, the oscillatory component $\widetilde{\phi}^\lambda_\sigma(E)$ describes local fluctuations of slopes of individual levels in a vicinity of E. (Note that an eventual weak dependence of $\widetilde{\phi}^\lambda_\sigma(E)$ on the large smoothing width Σ is suppressed in the notation.) One may readily anticipate that large absolute values $|\widetilde{\phi}^\lambda_\sigma(E)|$ indicate "*turbulent*" type of level dynamics (implying a large local frequency of avoided crossings of energy levels), whereas small values of $|\widetilde{\phi}^\lambda_\sigma(E)|$ can be associated with prevailingly "*laminar*" type of level dynamics (with a reduced occurrence of avoided crossings). With the aid of the Hellmann–Feynman formula, the flow rates from Eqs. (3)–(5) can be expressed via the substitution:

$$\frac{dE^\lambda_i}{d\lambda} = \left\langle \psi^\lambda_i \left| \frac{d\hat{H}^\lambda}{d\lambda} \right| \psi^\lambda_i \right\rangle = \int d^f\vec{x}\, |\psi^\lambda_i(\vec{x})|^2 \, \frac{\partial V^\lambda(\vec{x})}{\partial\lambda}, \tag{6}$$

where $\psi^\lambda_i(\vec{x})$ stands for wave functions of individual energy eigenstates. In this way, the flow rate quantities probe the distribution of quantum averages of operator $\frac{d}{d\lambda}\hat{H}^\lambda$ in the Hamiltonian eigenstates around energy E.

Reiteration of the procedure from part I yields the continuity equation for the total flow rate and total state density. It reads as:

$$\frac{\partial}{\partial\lambda}\left[\bar{\rho}^\lambda_\Sigma(E) + \widetilde{\rho}^\lambda_\sigma(E)\right] + \frac{\partial}{\partial E}\left[\bar{\rho}^\lambda_\Sigma(E)\bar{\phi}^\lambda_\Sigma(E) + \bar{\rho}^\lambda_\Sigma(E)\widetilde{\phi}^\lambda_\sigma(E) + \widetilde{\rho}^\lambda_\sigma(E)\bar{\phi}^\lambda_\Sigma(E) + \widetilde{\rho}^\lambda_\sigma(E)\widetilde{\phi}^\lambda_\sigma(E)\right] = 0. \tag{7}$$

This equation can be reduced by utilizing the continuity equation for the smooth components (Eq. (24) in part I). Assuming further that both oscillatory components $\widetilde{\rho}^\lambda_\sigma(E)$ and $\widetilde{\phi}^\lambda_\sigma(E)$ are small relative to the corresponding smooth components $\bar{\rho}^\lambda_\Sigma(E)$ and $\bar{\phi}^\lambda_\Sigma(E)$, one can neglect the "second-order" term $\widetilde{\rho}^\lambda_\sigma(E)\widetilde{\phi}^\lambda_\sigma(E)$. The resulting differential equation can be formally solved to approximate the oscillatory flow rate by the following expression:

$$\widetilde{\phi}^\lambda_\sigma(E) \approx \frac{1}{\bar{\rho}^\lambda_\Sigma(E)}\left[\text{const} - \widetilde{\rho}^\lambda_\sigma(E)\bar{\phi}^\lambda_\Sigma(E) - \int_{E_0}^{E} dE' \, \frac{\partial\widetilde{\rho}^\lambda_\sigma(E')}{\partial\lambda}\right]. \tag{8}$$

The integration constant inside the parentheses could, in principle, be determined from the required condition $\langle\widetilde{\phi}^\lambda_\sigma(E)\rangle = 0$ of zero energy average of the oscillatory rate. Formula (8) shows that large

oscillations of the state density and/or their strong variation with the control parameter tend to produce large values of the oscillatory flow rate, hence a more turbulent flow of levels.[1] On the other hand, small oscillations of the state density tend to generate more laminar flow, with prevailingly small values of the oscillatory flow rate.

Concerning thermodynamic consequences of the oscillatory state density, we again start from the results presented in part I (Section 2.4) and proceed in a similar way as above. First note that the total partition function $Z^\lambda(\beta)$ is well approximated by its smooth component $\bar{Z}^\lambda(\beta) \equiv \int dE\, \bar{\rho}^\lambda(E) \exp(-\beta E)$. This is because the integral defining the oscillatory component $\widetilde{Z}^\lambda(\beta) \equiv \int dE\, \widetilde{\rho}^\lambda(E) \exp(-\beta E)$ nearly vanishes due to the sign alternations of $\widetilde{\rho}^\lambda(E)$. As a consequence, the total thermal distribution of energy is given by:

$$w_\beta^\lambda(E) \approx \underbrace{\bar{\rho}^\lambda(E) \frac{e^{-\beta E}}{\bar{Z}^\lambda(\beta)}}_{\bar{w}_\beta^\lambda(E)} + \underbrace{\widetilde{\rho}^\lambda(E) \frac{e^{-\beta E}}{\bar{Z}^\lambda(\beta)}}_{\approx \widetilde{w}_\beta^\lambda(E)}, \tag{9}$$

where we again identify simple expressions of both smooth and oscillatory components.

It is clear from Eq. (9) that the oscillatory state density produces proportional oscillations of the thermal energy distribution. These oscillations may (are likely to) produce a number of tiny maxima and minima on the curve $w_\beta^\lambda(E)$, and therefore to affect the microcanonical inverse temperature $\beta^\lambda(E) = \frac{\partial}{\partial E} \ln \rho^\lambda(E)$, which is derived from the condition of zero derivative of the thermal energy distribution [1]. On the assumption of very small state-density oscillations, $\widetilde{\rho}^\lambda(E) \ll \bar{\rho}^\lambda(E)$, the microcanonical inverse temperature can be roughly estimated by:

$$\beta^\lambda(E) \approx \underbrace{\frac{\partial}{\partial E} \ln \bar{\rho}^\lambda(E)}_{\bar{\beta}^\lambda(E)} + \underbrace{\frac{1}{\bar{\rho}^\lambda(E)} \frac{\partial \widetilde{\rho}^\lambda(E)}{\partial E}}_{\approx \widetilde{\beta}^\lambda(E)}. \tag{10}$$

Here, the oscillatory inverse temperature $\widetilde{\beta}^\lambda(E)$ determines an eventual appearance of local minima and maxima in $w_\beta^\lambda(E)$ around the extremes of $\bar{w}_\beta^\lambda(E)$. This approximation implicitly assumes that the oscillatory distortions of the thermal energy distribution are not large enough to produce local minima or maxima away from the undisturbed extremes.

2.3. Periodic orbit approximation

Although, as discussed above, the oscillatory component of the state density represents just a finite-size effect, its origin can be traced back to the $\aleph \to \infty$ (classical) properties of the system. This essential insight follows from the so-called periodic-orbit approximation, which makes it possible to express $\widetilde{\rho}^\lambda(E)$ through classical periodic orbits. Here we just briefly recall the essence of this approximation. A detailed but accessible overview can be found, e.g., in the monographs [10,11].

The periodic-orbit formula for the oscillatory component of the state density exists in two forms, the so-called Gutzwiller formula [12] for systems with isolated periodic orbits (e.g., for chaotic systems), and the so-called Berry–Tabor formula [13] for systems with nonisolated periodic orbits (i.e., for typical regular systems). In both these implementations, the formula has the following general form:

$$\widetilde{\rho}^\lambda(E) \approx \frac{1}{\pi\hbar} \sum_o \sum_{r=1}^{\infty} \frac{T_o^\lambda(E)}{C_{ro}^\lambda(E)} \cos\left[\frac{r I_o^\lambda(E)}{\hbar} - \phi_{ro}^\lambda\right], \tag{11}$$

where the sums run over all primitive periodic orbits, identified by index o, and over their multiple repetitions $r = 1, 2, \ldots$. The quantity $I_o^\lambda(E)$ in the cosine argument represents an action along the

[1] Note that even large values of $\widetilde{\rho}_\sigma^\lambda(E)$ do not suffice to produce large $\widetilde{\phi}_\sigma^\lambda(E)$ if $\bar{\phi}_\Sigma^\lambda(E) \approx 0$ and $\frac{\partial}{\partial\lambda} \widetilde{\rho}_\sigma^\lambda(E) \approx 0$ or in case of an approximate cancellation of the three terms inside the parenthesis in Eq. (8).

given primitive orbit (for fixed parameter λ and energy E):

$$I_o^\lambda(E) = \oint_{o(\lambda,E)} \vec{p}\cdot d\vec{x}. \tag{12}$$

It is assumed that each orbit o exists within a certain energy interval, in which the variation of its action with energy contributes to the oscillations of $\widetilde{\rho}^\lambda(E)$. In contrast, the phase shift ϕ_{ro}^λ associated with r loops around o is energy-independent.

The amplitude of each oscillatory contribution is proportional to the period of the corresponding primitive orbit, $T_o^\lambda(E)$, and inversely proportional to the quantity $C_{ro}^\lambda(E)$, which is specified separately for chaotic and integrable systems. It reads as

$$C_{ro}^\lambda(E) = \begin{cases} \sqrt{|\det[(\mathbf{M}_o^\lambda)^r - \mathbf{1}]|} & \text{chaotic case,} \\ \sqrt{2\pi\hbar(r\mu_{o2})^3 \left|\dfrac{\partial}{\partial I_1}\mathcal{R}^\lambda(E,I_1)\right|_o} & \text{integrable case (for } f=2\text{).} \end{cases} \tag{13}$$

For a *chaotic system*, this quantity measures the stability of the full orbit, with $\mathbf{M}_o^\lambda$ standing for the monodromy matrix of the primitive orbit o and $\mathbf{1}$ for the unit matrix. The monodromy matrix quantifies, in a linearized form, the deviations of orbits with slightly shifted initial conditions from the unperturbed orbit o after a single cycle. The square root in the upper line of Eq. (13) yields values $\in [0, 2]$ for regular (stable) orbits and $\in [0, \infty]$ for chaotic (unstable) orbits [11]. Therefore, a stable orbit is expected to make in average a larger contribution to the sum (11) than a typical chaotic orbit.

On the other hand, in an *integrable system* all orbits are stable in the Lyapunov sense. These orbits are localized on manifolds which are topologically equivalent to tori [14]. For $f = 2$, any such torus is characterized by a pair of canonical actions (I_1, I_2), while the associated angle variables (φ_1, φ_2) specify the position on the torus. The variable $\mathcal{R}^\lambda = T_2^\lambda/T_1^\lambda$, appearing in Eq. (13), represents a ratio of periods corresponding to basic cycles in φ_1 and φ_2 (the ratio is expressed as a function of energy E and action I_1). For periodic orbits, this ratio has to take rational values, $\mathcal{R}^\lambda = \mu_{o1}/\mu_{o2}$, so that the incommensurable integers (μ_{o1}, μ_{o2}) characterize the given primitive orbit o. Its period is $T_o^\lambda = \mu_{o1}T_1^\lambda = \mu_{o2}T_2^\lambda$. The expression in the second line of Eq. (13) therefore quantifies the variation of the basic period ratio when one proceeds from the reference torus with trajectory o to the neighboring ones. In analogy with the chaotic case, "more stable" orbits (with smaller changes of the ratio $\mathcal{R}^\lambda$) give larger contribution to the sum (11).

We stress that the periodic-orbit approximation holds increasingly well as the limit $\hbar \to 0$ is approached. Formula (11) then expresses the emergence of discretized energy spectrum on the quantum side of the semiclassical borderline. As discussed below, the oscillatory effects studied in this work require to go beyond this approximation.

3. Creagh–Whelan model

In this section, we set the form and describe some properties of the 2D Creagh–Whelan (CW) model, that will be employed below in the numerical part of this paper (the model was used already in part I). We start by reviewing the parameter dependent family of CW Hamiltonians in Section 3.1, pointing out some features that will become relevant for the ESQPT precursors. One of such features is the proportion between regular and chaotic dynamics, which is broadly mapped in Section 3.2.

3.1. Hamiltonian forms

As in part I, we focus here on the systems described by Hamiltonians of the general form $\hat{H}^\lambda = \vec{p}^{\,2}/2 + V^\lambda(\vec{x})$, where $\vec{x}$ and $\vec{p}$ are f-dimensional coordinates and momenta and $V^\lambda(\vec{x})$ denotes a general analytic potential depending on a control parameter $\lambda \in \mathbb{R}^1$. All quantities appearing here and in the following expressions are *dimensionless*, which is achieved by convenient scaling of coordinates, momenta, and energy. The coordinate and momentum scales x_0 and p_0 together with the Planck

Table 1
Various parameter sets of the CW Hamiltonian (14) employed within this work. Some features of each set are pointed out, as well as a complete list of the figures in which the particular set was used.

Parameter set	B	C	D	Relative rigidity	Properties	Figures
#1	0	0.2	0.2	$R^0 \doteq 0.32$	$-A \leftrightarrow +A$ symmetric y-soft, mildly chaotic	1(a), 2(a), 8(a)
#2	0	30	10	$R^0 \doteq 3.2$	$-A \leftrightarrow +A$ symmetric y-rigid, semiregular	1(b), 2(b), 8(b), 9(a), 12(d), 10(a)–(c)
#3	0	39	1	$R^0 \doteq 3.2$	$-A \leftrightarrow +A$ symmetric y-rigid, highly chaotic	1(c), 2(c), 8(c), 9(b), 12(e), 10(d)
#4	39	20	20	$R^0_+ \doteq 4.4$, $R^0_- \doteq 0.5$	$-A \leftrightarrow +A$ asymmetric highly chaotic	1(d), 2(d), 3, 6(b), 8(d), 9(c), 12(a)–(c), 13
#5	0	0	0.4	$R^0 \doteq 0.32$	$-A \leftrightarrow +A$ symmetric y-soft, integrable	5(a)
#6	0	0	4	$R^0 \doteq 1$	$-A \leftrightarrow +A$ symmetric balanced, integrable	5(b)
#7	0	0	40	$R^0 \doteq 3.2$	$-A \leftrightarrow +A$ symmetric y-rigid, integrable	5(c), 6(a), 7

constant $\hbar$ can be combined into a dimensionless parameter $\aleph = p_0 x_0/\hbar$, which turns out to play the role of the system's size parameter [1]. In the following, we will use the bare identity $\aleph \equiv \hbar^{-1}$.

As discussed in part I, the above form of the Hamiltonian – with just the simplest quadratic (and coordinate-independent) kinetic term – does not in general express more complex Hamiltonians, that follow from the coordinate–momentum representation of many-body systems with f collective degrees of freedom. Nevertheless, we believe that the simpler case studied here shows the essentials of the problem and is a good starting point for more sophisticated analyses, that will follow.

We will again utilize the quadratic version of the generalized Creagh–Whelan potential [15], which was introduced and discussed in part I (see Section 3.1 there). This potential generates rather rich classical dynamics and makes it possible to illustrate various effects related to ordered and chaotic dynamics. The full Hamiltonian reads as:

$$\hat{H}^\lambda = -\frac{1}{2\aleph^2}\left(\frac{\partial^2}{\partial x^2} + \frac{\partial^2}{\partial y^2}\right) + \underbrace{(x^2-1)^2 + \overbrace{A}^{\equiv\lambda} x + Bxy^2 + Cx^2y^2 + Dy^2}_{V^\lambda(x,y)}, \tag{14}$$

where the role of control parameter λ is played by the coefficient $A \in (-\infty, +\infty)$ of the potential. We know from part I that this parameter drives the system through the first-order ground state phase transition at $A = 0$, where energies E_0^λ and E_1^λ of the lower and higher minimum become equal and swap. The minima are located at points $(x, y) = (x^\lambda_{0\pm}, 0)$ (the $x < 0$ minimum is higher for $A < 0$ and lower for $A > 0$, and vice versa) and are separated by a saddle point at $(x, y) = (x^\lambda_{\mathrm{sad}}, 0)$ with energy E^λ_{sad}. The remaining coefficients B, C, and D are additional parameters, which will enable us to tune the Hamiltonian along the scale between regular and chaotic dynamics. In this work, we will repeatedly utilize several choices of these parameters; these choices are listed in Table 1. Note that the additional parameters have to satisfy the conditions $B^2 \leq 4CD$ and $D > 0$, which guarantee that the potential is confining.

From the viewpoint of the forthcoming analysis, an important property of Hamiltonian (14) is a ratio between the x- and y-mode frequencies of vibrations around both minima of the potential. This property results from the harmonic approximation (valid for small-amplitude vibrations) of the CW potential in a vicinity of the respective minimum. The frequencies are given by:

$$\Omega^\lambda_{x\pm} = \sqrt{\frac{\partial^2 V^\lambda}{\partial x^2}}\bigg|_{(x^\lambda_{0\pm},0)}, \qquad \Omega^\lambda_{y\pm} = \sqrt{\frac{\partial^2 V^\lambda}{\partial y^2}}\bigg|_{(x^\lambda_{0\pm},0)}, \tag{15}$$

where the derivatives are taken at the global or local minimum, $(x, y) = (x^\lambda_{0\pm}, 0)$. Frequencies associated with these minima are depicted in Fig. 1 as functions of the control parameter A for four selected

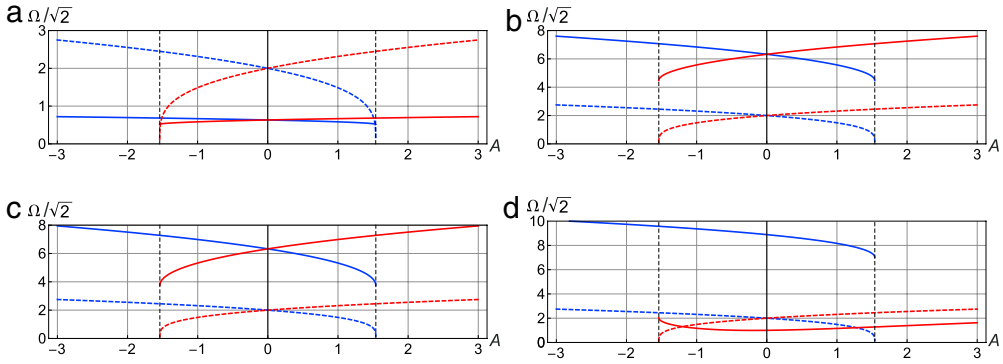

Fig. 1. (Color online) Frequencies of small-amplitude vibrations around the $x < 0$ and $x > 0$ minima of the CW potential from Eq. (14) with varying control parameter $\lambda \equiv A$ (horizontal axes) for parameter sets #1 (panel a), #2 (panel b), #3 (panel c), and #4 (panel d), see Table 1. The dashed curves correspond to the x-mode frequencies $\Omega^{\lambda}_{x\pm}$ in both minima (these are $-A \leftrightarrow +A$ symmetric and independent of B, C, D), while the full curves depict the y-mode frequencies $\Omega^{\lambda}_{y\pm}$. Vertical dashed lines demarcate spinodal points $A = \pm\sqrt{64/27}$, where the respective secondary minimum of the potential disappears.

combinations of additional parameters B, C and D. Later it will become important to distinguish various forms of the CW potential with respect to the ratio of the x and y frequencies. Since the ratio varies with A, we take the value at $A = 0$ (where $\Omega^0_{x-} = \Omega^0_{x+} = 2\sqrt{2}$):

$$R^0_{\pm} = \frac{\Omega^0_{y\pm}}{\Omega^0_{x\pm}} = \frac{\sqrt{\pm B + C + D}}{2}. \tag{16}$$

In the symmetric case ($B = 0$), the frequencies at $A = 0$ are equal for both wells, hence $R^0_{\pm} \equiv R^0$. The ratio in Eq. (16), hereafter called relative rigidity, will be used to schematically classify the potentials as *y-rigid* (with $R^0_{\pm} > 1$), *y-soft* (with $R^0_{\pm} < 1$), *balanced* (with $R^0_{\pm} \approx 1$), and *asymmetric* (with $R^0_{-} \gtrless 1 \gtrless R^0_{+}$). Relative rigidities of the potential forms used throughout this work are given in Table 1. It should be stressed that realistic time scales of motions in both x and y directions depend in general not only on all parameters A, B, C, D, but also on energy E. In this sense, the relative rigidity in Eq. (16) provides only a rough quantification, which is relevant only in a limited energy domain.

An essential special case of Hamiltonian (14) is that with $B = C = 0$:

$$\hat{H}^{\lambda} = \underbrace{\left(-\frac{1}{2\aleph^2}\frac{\partial^2}{\partial x^2} + \overbrace{x^4 - 2x^2 + Ax + 1}^{V^{\lambda}_x(x)}\right)}_{\hat{H}^{\lambda}_x} + \underbrace{\left(-\frac{1}{2\aleph^2}\frac{\partial^2}{\partial y^2} + \overbrace{Dy^2}^{V_y(y)}\right)}_{\hat{H}_y}. \tag{17}$$

This Hamiltonian represents a fully *integrable* system, in which the x and y degrees of freedom are separated. The integrability is guaranteed by the obvious fact that the 1D Hamiltonians corresponding to the x- and y-motions commute: $[\hat{H}^{\lambda}_x, \hat{H}_y] = 0$. Both these observables are conserved (they commute with the full Hamiltonian $\hat{H}$) and, on a classical level, their gradients in a 4-dimensional phase space are perpendicular (thus linearly independent, as required in the definition of an integrable system [14]).

3.2. Order–chaos competition

Any nonzero choice of parameters B and C of the Hamiltonian (14) produces dynamics somewhere in between order and chaos. The degree of chaos depends in general on all Hamiltonian parameters A, B, C, D, as well as on energy E. To quantify the regular/chaotic content of the system, we use a

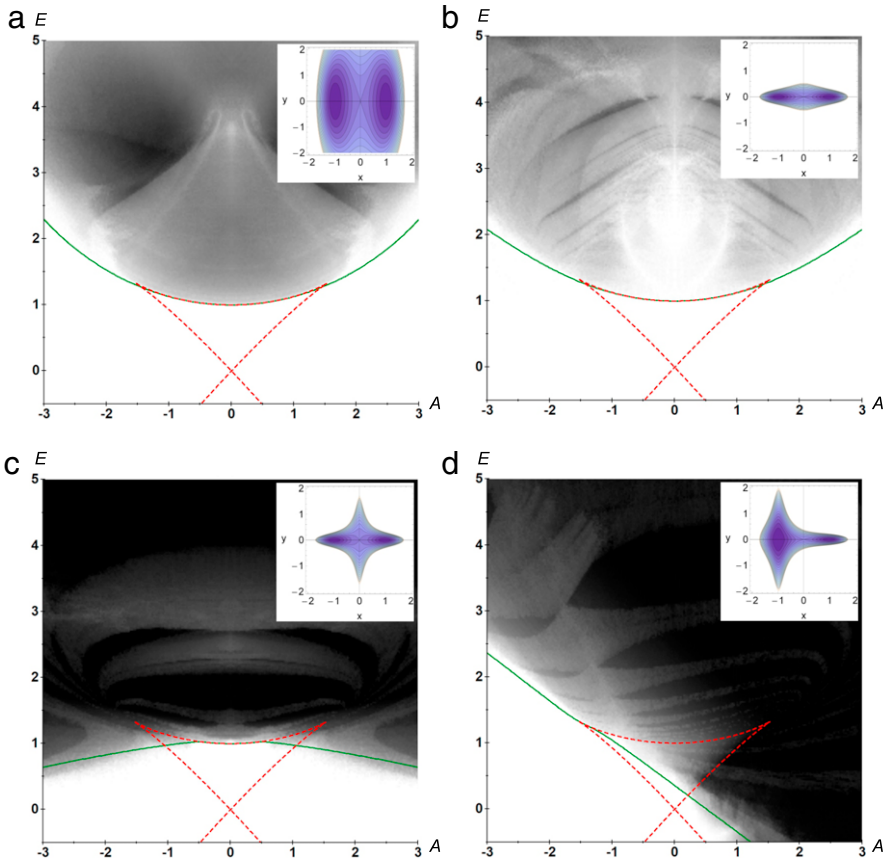

Fig. 2. (Color online) Maps of the regular fraction $f^{\lambda}_{\rm reg}(E)$ from Eq. (18) in the $\lambda \times E$ plane for Hamiltonian (14) with parameter sets #1 (panel a), #2 (panel b), #3 (panel c), and #4 (panel d). The value of $f_{\rm reg}$ is coded by the degree of gray—white corresponds to perfect order ($f_{\rm reg} = 1$) and black to full chaos ($f_{\rm reg} = 0$). Dashed curves mark energies of stationary points of the potential. The full curve indicates an expected energy $E^{\lambda}_{\rm ch}$ for the onset of chaos—see text. The respective potentials for $A = 0$ are shown in the insets.

so-called regular fraction, which is defined as:

$$f^{\lambda}_{\rm reg}(E) = \frac{\mathcal{S}^{\lambda}_{\rm reg}(E)}{\mathcal{S}^{\lambda}_{\rm tot}(E)}, \quad \mathcal{S}^{\lambda}_{\rm tot}(E) = \int \cdots \int d^f\vec{p}\, d^f\vec{x}\, \delta\big[E - H^{\lambda}(\vec{p},\vec{x})\big] \propto \bar{\rho}^{\lambda}(E). \tag{18}$$

This quantity represents a fraction of the phase space filled with regular orbits relative to the total phase space available at energy E, that is, a $(2f-1)$-dimensional surface "area" $\mathcal{S}^{\lambda}_{\rm reg}(E)$ of the regular part of the given energy shell relative to the total available area $\mathcal{S}^{\lambda}_{\rm tot}(E)$. Clearly, the regular fraction is a number between 0 (corresponding to total chaos) and 1 (perfect order). The procedure for evaluating $f_{\rm reg}$ consists in a generation of orbits with initial conditions randomly distributed on the energy shell and in an efficient resolution of their regular or chaotic character. For general $f = 2$ systems it is described in Ref. [16]. The $\lambda \times E$ maps of the regular fraction characterizing the CW Hamiltonian with parameter sets from #1 to #4, see Table 1, are given in Fig. 2. Note that $f_{\rm reg}$ in this figure was numerically determined only from trajectories passing the $y = 0$ section of the phase space.

Since small-amplitude motions around the global quadratic minimum of the potential are nearly harmonic, the dynamics is always almost fully regular for sufficiently low excitation energies $E < E_{\rm ch}$. This is seen in Fig. 2. An efficient *heuristic* (hence imperfect) criterion to estimate the "critical" energy $E_{\rm ch}$, where first chaotic orbits occur, was discussed in Ref. [17]. For system with Hamiltonian

$\hat{H} = \vec{p}^{\,2}/2 + V(\vec{x})$, the criterion is based on concavity/convexity of the potential energy contours in the configuration space (or surfaces, for $f > 2$). It can be formulated as follows (for $f = 2$): if all potential energy contours $V(x, y) = \text{const} < E$ below a selected value E are convex, the system with energy E is likely to be prevailingly regular: $f_{\text{reg}}(E) \approx 1$. Chaos starts propagating at energy $E = E_{\text{ch}}$ where the first partly concave contour appears. This is when the shape of the energetically accessible domain in the $x \times y$ plane develops a concave segment. For energies above E_{ch} we generally expect either partial, or full chaos: $f_{\text{reg}}(E) < 1$.[2]

In Fig. 2, the dependence E^{λ}_{ch} of the anticipated low-energy bound of chaos on the control parameter $\lambda \equiv A$ is indicated by the full curve in each panel. The expectations formulated in the preceding paragraph are roughly verified, although partly chaotic dynamics sometimes appears even below E^{λ}_{ch} and, vice versa, almost regular dynamics appears well above E^{λ}_{ch}. In some cases (panels (a) and (b)), the dependence E^{λ}_{ch} in the spinodal region of the control parameter is rather close to the energy of the saddle point separating the coexisting minima. The corresponding ESQPT critical energy E^{λ}_{c} then almost precisely coincides with the onset of chaos. However, this coincidence should be considered as a mere accident—it apparently does not apply in a general situation, as seen in panels (c) and (d). The form of the CW potential for the given choice of parameters is depicted in the corresponding inset of Fig. 2 (all potentials are drawn for $A = 0$). One can see that more chaotic dynamics (panels (c) and (d)) is associated with potentials having more concave contours than the potentials generating less chaotic dynamics (panels (a) and (b)). Therefore, the above outlined general phenomenology turns out to be qualitatively functioning in the cases studied.

Fig. 3 shows some Poincaré maps corresponding to fully/partly regular as well as fully chaotic dynamics of the CW system. The choice of Hamiltonian parameters B, C, D is the same as in panel (d) of Fig. 2, the values of parameter A and energy E are selected as indicated in the figure. The maps display trajectories crossing the $y = 0$ line of the coordinate plane—each crossing leaves a point in the plane coordinate $x \times$ momentum p_x (while p_y is fixed by the value of E). Whereas points collecting on regular curves indicate regular motions (deformed tori in the phase space [14]), an "ergodic mesh" of points signals chaotic dynamics. Let us stress that the Poincaré maps in Fig. 3 are in perfect agreement with the dependence of $f^{\lambda}_{\text{reg}}(E)$ presented in Fig. 2(d). They moreover provide a detailed information on the nature of mixed dynamics for some values of parameters and energy, allowing one to visualize the regular and chaotic domains of the phase space.

4. Integrable (separable) dynamics

In this section, we focus on the integrable version of the CW Hamiltonian, which is given in Eq. (17). Before showing results of our numerical analysis (Section 4.2), we make some general remarks on the state density in separable systems (Section 4.1).

4.1. General analysis

A general *separable* Hamiltonian $\hat{H}$ with two degrees of freedom, which are represented by the (coordinate, momentum) pairs of operators $(\hat{x}, \hat{p}_x)$ and $(\hat{y}, \hat{p}_y)$, can be written as:

$$\hat{H} = H[\hat{p}_x, \hat{x}, \underbrace{G_y(\hat{p}_y, \hat{y})}_{\hat{G}_y}], \tag{19}$$

where $H[*, *, *]$ stands for an arbitrary (assumingly "well behaved") function of three variables and $\hat{G}_y$ represents an operator connected solely with the y degree of freedom. We immediately verify that $[\hat{H}, \hat{G}_y] = 0$, obtaining two mutually compatible integrals of motions that guarantee the integrability of the $f = 2$ problem. The full 2D stationary Schrödinger equation $\hat{H}|\psi\rangle = E|\psi\rangle$ is solved with separate state vectors of the form $|\psi\rangle = |\psi_x(n_x, n_y)\rangle|\psi_y(n_y)\rangle$, where (n_x, n_y) stands for a pair of quantum

[2] Islands of regular dynamics above E_{ch} can be caused by some cancellation effect involving convex and concave contours [17]. For certain polynomial potentials the dynamics may become increasingly regular at very high energies, where the motions are effectively controlled only by the highest-power potential terms.

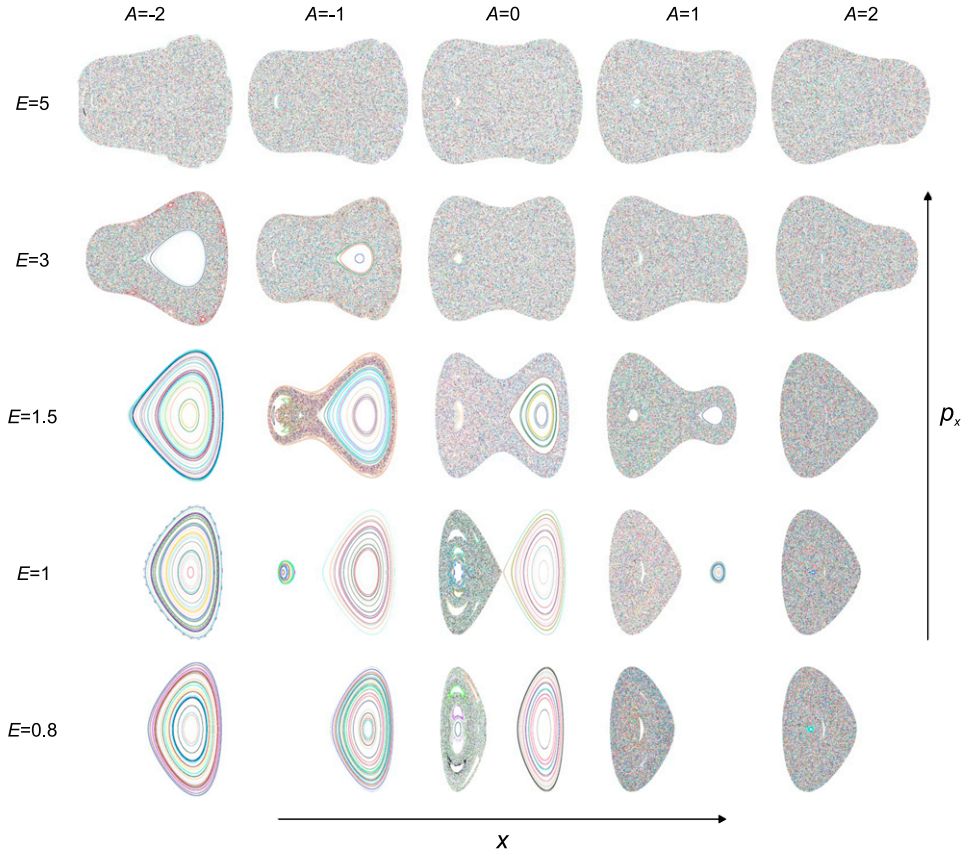

Fig. 3. (Color online) Poincaré maps of the CW Hamiltonian with parameter set #4 (cf. Fig. 2(d)). Energy E and the value of parameter A are assigned to individual maps on the left and upper margins. Each map is composed of the total number of 10^5 passages (points in the plane $x \times p_x$) of 50 randomly chosen trajectories through the $y = 0$ phase-space section.

numbers characterizing the spectrum. The vector $|\psi_y(n_y)\rangle$ is a solutions of 1D eigenvalue equation $\hat{G}_y|\psi_y(n_y)\rangle = g(n_y)|\psi_y(n_y)\rangle$. The corresponding vector $|\psi_x(n_x, n_y)\rangle$ is obtained via replacing the operator $\hat{G}_y$ in Eq. (19) by the constant $g(n_y)$ and solving the associated effective 1D Schrödinger equation. This procedure generally results in some selection rules specifying the allowed combinations of quantum numbers (n_x, n_y).

The most important implication of the above type of separability is the existence of repeated multiplets of levels in the spectrum $E(n_x, n_y)$ of the full Hamiltonian $\hat{H}$. To be specific, let us assume that the typical spacing $\Delta E_y \equiv [E(n_x, n_y + 1) - E(n_x, n_y)]$ is much larger than $\Delta E_x \equiv [E(n_x + 1, n_y) - E(n_x, n_y)]$, hence $\Delta E_y \gg \Delta E_x$. Then each $g(n_y)$ eigensolution of $\hat{G}_y$ generates a band of eigenstates of the full Hamiltonian differing by values of the n_x quantum number (within the subset allowed with respect to the given n_y). Each of these bands carries patterns characterizing the 1D Schrödinger equation with effective Hamiltonian $H[\hat{p}, \hat{x}, g(n_y)]$. If this Hamiltonian for a certain sequence of $g(n_y)$ eigenvalues (a set of n_y quantum numbers) exhibits an ESQPT, its signatures will appear *repeatedly* in each band associated with the given $\{n_y\}$ set. Moreover, the ESQPT signatures observed in each of these "replicas" are *stronger* than would be expected for an $f = 2$ problem, because they originate in the 1D effective Hamiltonian $H[\hat{p}, \hat{x}, g(n_y)]$. On the other hand, the $\hbar \to 0$ limit reduces the separation of individual bands to zero, making the ESQPT multiplication and enhancement phenomenon disappear. This phenomenon is therefore just a *finite-size effect*.

A more detailed analysis of the effects of separability on the ESQPT precursors depends on the specific system under consideration. In particular, one needs to decide concerning the presence or absence of ESQPT in effective Hamiltonians $H[\hat{p}_x, \hat{x}, g(n_y)]$ with different values of $g(n_y)$.[3] To demonstrate the separability effects in their simplest and most spectacular form, we consider in this subsection a trivial type of $f = 2$ separable Hamiltonian, which reads as:

$$\hat{H} = H_x(\hat{p}_x, \hat{x}) + H_y(\hat{p}_y, \hat{y}). \tag{20}$$

In this case, the eigensolutions associated with both x and y directions are completely independent and all combinations of (n_x, n_y) are possible. A separable Hamiltonian of this form is realized within the family of Creagh–Whelan potentials, see Eq. (17). The component $\hat{H}_y$ represents just a harmonic oscillator with spectrum given by $E_y(n_y) = \hbar\Omega_y(n_y + 1/2)$, where $\Omega_y = \sqrt{2D}$ and $n_y = 0, 1, 2, \ldots$. Note that we have $\hbar \equiv \aleph^{-1}$, both values being used interchangeably below. The component $\hat{H}_x^\lambda$ coincides with the Hamiltonian of the quantum cusp catastrophe [18], with potential $V_{\mathrm{cusp}}(x) = x^4 + ax + bx^2 + c$, where we substitute $a = A \equiv \lambda$, $b = -2$, and $c = 1$. The spectrum $E_x^\lambda(n_x)$ of the cusp Hamiltonian ($n_x =$ integer) was analyzed numerically, with respect to the ESQPT structures, in Ref. [4] and also in part I of this series.

Since the total energy of the separable Hamiltonian (20) is a sum of energies corresponding to the x- and y-motions, one can construct the full quantum spectrum by a convolution of the two partial spectra: $E^\lambda(n_x, n_y) = E_x^\lambda(n_x) + E_y(n_y)$. In particular, the total density $\rho^\lambda(E) = \sum_{n_x,n_y} \delta[E - E^\lambda(n_x, n_y)]$ of energy eigenstates is given by:

$$\begin{aligned}\rho^\lambda(E) &= \int_{-\infty}^{\infty}\int_{-\infty}^{\infty} dE_x dE_y\, \delta(E_x + E_y - E)\, \rho_x^\lambda(E_x)\rho_y(E_y) \\ &= \int_{-\infty}^{\infty} dE_x\, \rho_x^\lambda(E_x)\rho_y(E - E_x),\end{aligned} \tag{21}$$

where $\rho_x^\lambda(E_x)$ and $\rho_y(E_y)$ stand for the state densities of the partial spectra corresponding to the respective 1D systems. Note that although the integration in Eq. (21) formally goes from $-\infty$, all spectra naturally have their lower bounds below which the corresponding densities vanish identically. For the CW Hamiltonian (17) the lower bound of the E_y spectrum is zero, while the lower bound of E_x and E will be denoted as E_0^λ.

The smooth component of the total state density is given by a convolution of the two partial smooth components, as can be easily verified from the following equality:

$$\begin{aligned}&\int dE_x \overbrace{\iint dp_x\, dx\, \delta[H_x(p_x, x) - E_x]}^{\frac{2\pi}{\aleph}\bar{\rho}_x^\lambda(E_x)} \overbrace{\iint dp_y\, dy\, \delta[H_y(p_y, y) - (E - E_x)]}^{\frac{2\pi}{\aleph}\bar{\rho}_y(E-E_x)} \\ &= \iiiint dp_x\, dp_y\, dx\, dy\, \delta[\underbrace{H_x(p_x, x) + H_y(p_y, y)}_{H(p_x,p_y,x,y)} - E] \equiv \left(\frac{2\pi}{\aleph}\right)^2 \bar{\rho}^\lambda(E),\end{aligned} \tag{22}$$

where $H_x(p_x, x)$, $H_y(p_y, y)$ and $H(p_x, p_y, x, y)$ are classical Hamiltonian functions. We observe that the convolution of both partial phase-space integrals yields the total phase-space integral, associated with the smooth component $\bar{\rho}^\lambda(E)$ of the total state density.

Eq. (22) can be easily used to calculate the smooth component $\bar{\rho}^\lambda(E)$ of the eigenstate density of the separable CW Hamiltonian (17). We know that the smooth component of the harmonic-oscillator state density is constant, independent of energy: $\bar{\rho}_y = \text{const}$. We also know the numerically determined form of the smooth component of the cusp state density—see Fig. 10(a) in Ref. [1]. In particular, we recall that $\bar{\rho}_x^\lambda$ exhibits a jump at the energy of the secondary minimum of the cusp potential in the

[3] A familiar example of the above mechanism is the creation of a centrifugal barrier. This may prevent some ESQPTs to affect states with non-zero angular momenta, cf. Ref. [2].

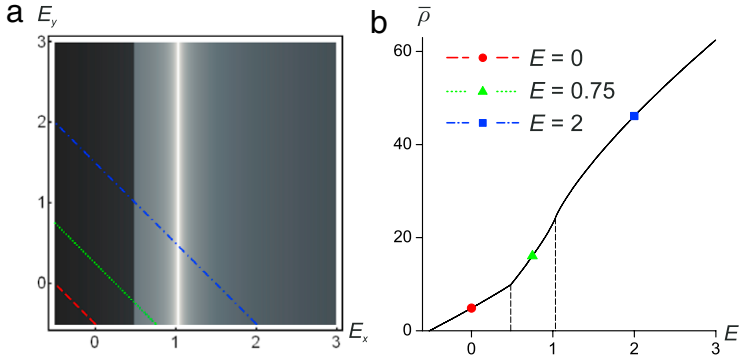

Fig. 4. (Color online) Evaluation of the smooth component of state density for the separable CW Hamiltonian (17) with $A = 0.5$ and $D = 1$. (a) Density plot of the product $\bar{\rho}_x(E_x)\bar{\rho}_y(E_y)$ with brighter (darker) shades indicating larger (smaller) values. Note the 1D ESQPT structures in $\bar{\rho}_x(E_x)$. The tilted lines visualize paths of the convolution integral for three values of total energy E. (b) The total density $\left(\frac{2\pi}{\aleph}\right)^2 \bar{\rho}(E)$ obtained by the convolution, see Eq. (22). Energies corresponding to the 3 lines from panel (a) are marked by dots, the ESQPT critical energies of the 2D system by vertical dashed lines.

spinodal region, and an infinite peak at the energy of the local maximum separating the two minima. The convolution of $\bar{\rho}_x^\lambda(E_x)$ and $\bar{\rho}_y(E_y)$ is depicted in Fig. 4. The resulting state density $\bar{\rho}(E)$ in panel (b) of this figure clearly exhibits the 2D ESQPT structures – the break and the vertical growth – associated, respectively, with the secondary minimum and with the saddle point of the potential $V^\lambda = V_x^\lambda + V_y$ from Eq. (17). Panel (a) depicts the state density in the plane $E_x \times E_y$. This panel makes clear how the 2D ESQPT structures follow – via the convolution integral – from the 1D structures associated with the cusp potential.

From Eqs. (21) and (22) we obtain the following exact relation for the oscillatory component $\widetilde{\rho}^\lambda(E) = \rho^\lambda(E) - \bar{\rho}^\lambda(E)$ of the total state density:

$$\widetilde{\rho}^\lambda(E) = \int_{-\infty}^{\infty} dE_x\, \bar{\rho}_x^\lambda(E_x)\, \widetilde{\rho}_y(E - E_x) + \int_{-\infty}^{\infty} dE_x\, \widetilde{\rho}_x^\lambda(E_x)\, \bar{\rho}_y(E - E_x) + \int_{-\infty}^{\infty} dE_x\, \widetilde{\rho}_x^\lambda(E_x)\, \widetilde{\rho}_y(E - E_x). \tag{23}$$

In a truly semiclassical case, the only contribution to $\widetilde{\rho}^\lambda(E)$ is given by the last term of this formula. The first two terms can be neglected because of generically fast (for $\aleph \to \infty$) oscillations of their subintegral functions around zero. The last term, in contrast, produces a non-negligible contribution through some "resonating" fragments of both x and y oscillatory state densities, which add up coherently in the resulting integral. Indeed, as shown in Appendix, the stationary-phase approximation applied to the last term in Eq. (23) recovers the periodic-orbit approximation (11) in dimension 2 for a separable system from the corresponding 1D formulas. As the attention of our work is focused on finite-size (not fully semiclassical) cases, formula (23) needs to be considered with all three terms.

A separable Hamiltonian of the form (20) allows for situations when the two separated degrees of freedom approach the classical limit in an *imbalanced* way, that is, with significantly different average time scales of motions in both directions. This implies strongly deviated cumulative densities $N_x = \int_{E_{0x}}^{E} \rho_x(E_x)dE_x$ and $N_y = \int_{E_{0y}}^{E} \rho_y(E_y)dE_y$, which represent the numbers of eigenstates of both 1D subsystems participating in the combined eigenstates of the whole system with total energy up to E. In the case of the CW Hamiltonian (at sufficiently low energies), the ratio of both time scales can be roughly quantified by the fraction $R^0 \equiv \Omega_y^0/\Omega_x^0$, that in an imbalanced situation yields a value either much smaller or much larger than unity. Then, to express effective classicality of the x and y subsystems, the single size parameter $\aleph$ characterizing the entire 2D system should be supplemented

by a pair of values $(\aleph_x, \aleph_y)$, obtained from separate scalings of both 1D subsystems.[4] This can be achieved by substitutions $x \mapsto x' = x/\sqrt{R^0}$ and $y \mapsto y' = \sqrt{R^0}y$ performed in Eq. (17), which leads to:

$$-\frac{1}{2\aleph^2}\left(\frac{\partial^2}{\partial x^2}+\frac{\partial^2}{\partial y^2}\right) \mapsto -\frac{1}{2\aleph_x^2}\frac{\partial^2}{\partial x'^2}-\frac{1}{2\aleph_y^2}\frac{\partial^2}{\partial y'^2}, \quad \text{with} \begin{cases} \aleph_x = \aleph\sqrt{R^0}, \\ \aleph_y = \aleph/\sqrt{R^0}. \end{cases} \tag{24}$$

In highly rigid or highly soft cases, the values of $\aleph_x$ and $\aleph_y$ differ substantially, therefore we may say that one degree of freedom is much closer to the classical limit than the other one. As a result, the conditions for the neglect of both mixed terms in Eq. (23) are not satisfied. Instead, the more rigid (faster) degree of freedom needs to be taken into account with its full density $\rho_* = \bar{\rho}_* + \widetilde{\rho}_*$ while the softer (slower) degree of freedom may be approximated just by the smooth component $\bar{\rho}_*$. This approximation follows from a crucial assumption, applied below, that the oscillatory component $\widetilde{\rho}_*$ of the softer degree of freedom is effectively *washed out* by the smoothing procedure with an appropriately set parameter σ. In other words, we choose to portray only the oscillatory effects related to the *rigid subsystem* since the soft subsystem is much closer to classicality. This leads to the following approximations:

(a) y-rigid case ($R^0 \gg 1$): The oscillatory component $\widetilde{\rho}_x^\lambda(E_x)$ oscillates much faster than $\widetilde{\rho}_y^\lambda(E_y)$ and can be neglected, hence only the first term of Eq. (23) works. Substituting an exact expression $\widetilde{\rho}_y(E_y) = \sum_{n_y} \delta\left[E_y - \hbar\Omega_y(n_y+\frac{1}{2})\right] - 1/\hbar\Omega_y$, we get:

$$\widetilde{\rho}^\lambda(E) \approx \sum_{n_y=0}^{\bar{n}_y^\lambda(E)} \bar{\rho}_x\left[E - \hbar\Omega_y\left(n_y+\tfrac{1}{2}\right)\right] - \frac{1}{\hbar\Omega_y}\int_{E_0^\lambda}^{E} dE_x\, \bar{\rho}_x(E_x), \tag{25}$$

where the upper summation value reads as $\bar{n}_y^\lambda(E) = \lfloor (E-E_0^\lambda)/\hbar\Omega_y - \frac{1}{2}\rfloor$, with $\lfloor * \rfloor$ denoting an integer part (floor function). The sum in the first term represents a staircase approximation of the integral in the second term (including the prefactor). The dependence (25) therefore has a sawtooth ("zig-zag") shape with apexes separated by $\Delta E = \hbar\Omega_y$, which is the plateau width of the staircase approximation. Similarly, the derivative $\frac{d}{dE}\rho^\lambda(E)$ exhibits periodic jumps. This behavior captures the trivial fact that the same dense spectrum of the cusp Hamiltonian $\hat{H}_x$ is built above each isolated oscillator level $E_y(n_y)$.

(b) y-soft case ($R^0 \ll 1$): The situation is analogous to the case (a), but with a swap of x and y degrees of freedom. Only the second term of Eq. (23) works, yielding:

$$\widetilde{\rho}^\lambda(E) \approx \frac{1}{\hbar\Omega_y}\int_{E_0^\lambda}^{E} dE_x\, \widetilde{\rho}_x^\lambda(E_x). \tag{26}$$

The full density $\rho^\lambda(E)$ is approximated by $N_x^\lambda(E)/\hbar\Omega_y$, where $N_x^\lambda(E)$ represents a number of cusp levels below energy E (cumulative state density). Therefore, the derivative $\frac{d}{dE}\rho^\lambda(E)$ peaks at every cusp level. The interpretation of this behavior is similar to case (a), namely, it reflects the fact that the same dense spectrum of the oscillator Hamiltonian $\hat{H}_y$ is built on each isolated cusp level $E_x(n_x)$.

4.2. Case study

Theoretical conclusions of the previous subsection will now be illustrated by numerical calculations based on the separable CW Hamiltonian (17). In order to clearly visualize the separability effects in the oscillatory components of the state density and flow rate, the value of smoothing parameter σ in Eqs. (2) and (5) needs to be taken somewhere in between average spacings of neighboring levels in the soft and rigid 1D subsystems. Level spacings for both x and y degrees of freedom should be properly determined from the respective average state densities, $\Delta E_*^\lambda \approx 1/\bar{\rho}_*^\lambda(E_*)$ with $* = x, y$, so

[4] Independent scaling of the x and y phase spaces yields $(\aleph_x, \aleph_y) \equiv \hbar^{-1}(p_0x_0, q_0y_0)$, with an additional constraint $\aleph_x\aleph_y = \aleph^2$ following from consistency with the $f = 2$ expression (see Section 2.1 of Ref. [1]).

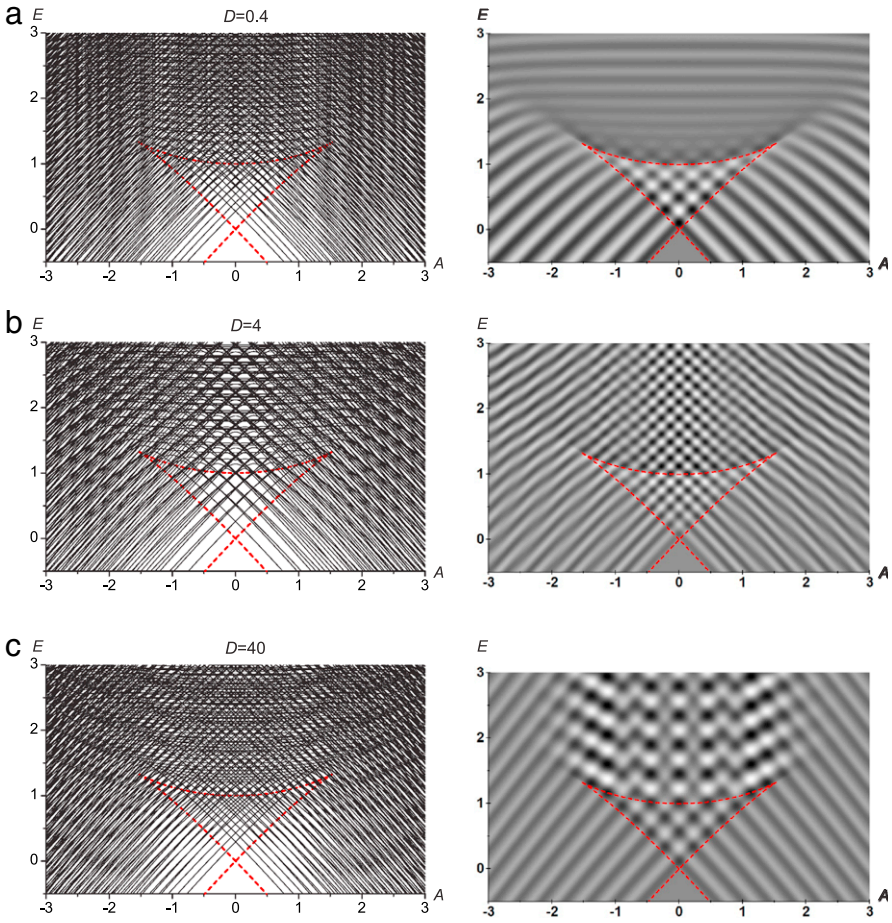

Fig. 5. Level dynamics and the oscillatory state density for the separable CW Hamiltonian (17) with parameter sets #5 (row a), #6 (row b) and #7 (row c). Oscillatory components $\widetilde{\rho}^{\lambda}_{\sigma}(E)$ shown in the right-hand panels were calculated via formula (2) from the respective exact spectrum in the left-hand panels. Bright (dark) shades of gray in the right-hand panels indicate positive (negative) values of $\widetilde{\rho}^{\lambda}_{\sigma}(E)$. Dashed curves mark stationary points of the potential. Size and smoothing parameters are taken as follows: (a) $\aleph = 20/3$, $\sigma = 0.09$, (b) $\aleph = 10$, $\sigma = 0.1$, (c) $\aleph = 20$, $\sigma = 0.1$.

they in general vary with λ and E_x or E_y. However, at lower energies, where the harmonic-oscillator approximation of both potential wells is good enough, the spacings are almost independent of energy, determined from the oscillator frequencies Ω^{λ}_x and Ω^{λ}_y. Using the frequency values at $\lambda \equiv A = 0$ (cf. Fig. 1), we can estimate both spacings by:

$$\Delta E^0_x \approx \frac{\Omega^0_x}{\aleph} = \frac{\sqrt{\Omega^0_x \Omega^0_y}}{\aleph_x}, \qquad \Delta E^0_y \approx \frac{\Omega^0_y}{\aleph} = \frac{\sqrt{\Omega^0_x \Omega^0_y}}{\aleph_y} \tag{27}$$

(remind: $\aleph^{-1} \equiv \hbar$). An empirically obtained optimal value of the smoothing parameter, which will be employed in almost all forthcoming figures of the oscillatory properties, is proportional to the *geometric average* of the above two spacings, namely: $\sigma \approx 0.4\sqrt{\Delta E^0_x \Delta E^0_y}$.

Fig. 5 shows raw spectra of energy levels E^{λ}_i and the corresponding oscillatory state density $\widetilde{\rho}^{\lambda}_{\sigma}(E)$ for the separable model (17) with three selected values of frequency $\Omega_y = \sqrt{2D}$ defining the y-rigidity

of the potential. The situations displayed in the three rows of Fig. 5 correspond to parameter sets #5, #6, and #7 from Table 1, i.e., to y-soft (row a), y-rigid (row c), and balanced (row b) cases. The left-hand panel in each row depicts the level dynamics (variation of the exact spectrum E_i^λ with parameter $A \equiv \lambda$), while the respective right-hand panel shows the oscillatory state density. To keep roughly the same number of levels in the energy region displayed in each panel, the overall size parameter $\aleph$ was taken differently in each row—specific values are again given in the figure caption. Let us note that level dynamics in left-hand panels of Fig. 5 is non-generic in the sense that many (although not all) of the observed crossings of levels are unavoided—that is, real. This is a trivial consequence of separability of the Hamiltonian which eliminates interaction between levels with different pairs of quantum numbers (n_x, n_y).

The effects demonstrated in the top and bottom rows of Fig. 5 are consistent with the anticipations formulated at the end of Section 4.1. In the y-rigid case (row c) one observes that the oscillatory component of the state density shows variations correlated with individual levels of the oscillator potential V_y. In particular, $\widetilde{\rho}_\sigma^\lambda(E)$ carries well distinguished ESQPT structures associated with the 1D cusp potential (its stationary points are located along the ∇-like profile in the figure), which are replicated equidistantly (period $\Delta E = \Delta E_y = \hbar\Omega_y$) with increasing excitation energy. On the other hand, in the y-soft case (row a) one recognizes variations of $\widetilde{\rho}_\sigma^\lambda(E)$ correlated with individual levels of the cusp potential V_x^λ. The oscillatory component thus displays just a single 1D cusp ESQPT structure, with no replication. The balanced case with comparable x and y frequencies (row b) leads to an oscillatory state density showing a regular interference pattern in the spinodal region, but no residual 1D ESQPT structures. Note that similar effects are present also in the $\lambda \times E$ dependences of the derivatives $\frac{d}{dE}\widetilde{\rho}_\sigma^\lambda(E)$ and $\frac{d}{dE}\rho_\sigma^\lambda(E)$ that we do not show here [19].

As we see in Fig. 5, the oscillatory state density $\widetilde{\rho}_\sigma^\lambda(E)$ contains resembling structures in both y-rigid and y-soft cases, in spite of their different origins. The similarity is due to the fact that the average spacing between levels of the rigid subsystem (ΔE_x^0 in row (a) and ΔE_y^0 in row (c)) was chosen about the same in both cases. This leads to similar patterns of oscillations inside and aside the spinodal ∇-like domain. However, both patterns differ for energies above the ∇-domain, where the y-soft potential does not develop the "checkered pattern" associated in the y-rigid case with the $\hbar\Omega_y$-spaced replicas of the ∇-domain.

A less apparent distinction between y-rigid and y-soft cases of level dynamics follows from a difference between the numbers of levels of the 1D cusp Hamiltonian $\hat{H}_x^\lambda$ that participate in the formation of the ESQPT precursors for the full CW Hamiltonian. This number is much larger in the y-rigid case than in the y-soft case. Because the 2D ESQPT precursors originate from 1D ESQPT properties of $\hat{H}_x^\lambda$, they should be "more developed" in the y-rigid case (e.g., in the sense of sharpness of avoided crossings of the cusp levels). Although this distinction is not very apparent in the present example, it may be relevant in more general cases. Considering specifically the case depicted in Fig. 5, we note that while in the y-rigid case the value of the effective size parameter for the critical subsystem is $\aleph_x \doteq 35.6$, in the y-soft case it is just $\aleph_x \doteq 3.7$ (these particular values follow from the given rigidity ratios R^0 and also from the different values of the overall size parameter $\aleph$ employed in both calculations). The density of the 1D cusp spectrum is therefore by an order of magnitude larger in the y-rigid case than in the y-soft case (though the total state density is about the same).

Panel (a) of Fig. 6 shows the oscillatory component $\widetilde{\phi}_\sigma^\lambda(E)$ of the flow rate calculated for the y-rigid separable Hamiltonian with parameter set #7 (the same as in row (c) of Fig. 5). One observes a pattern of flow-rate oscillations which is very similar to the pattern of level-density oscillations. An apparent difference between both Figs. 6(a) and 5(c) is that the flow-rate oscillations are odd with respect to the inversion of the parameter axis, while the level-density oscillations are even—both these features follow directly from the $+A \leftrightarrow -A$ symmetry of the problem. Similar relation between oscillatory state density and flow rate would be established also for other choices of the Hamiltonian parameters, but these are not shown here (Fig. 6(b) corresponds to a chaotic Hamiltonian discussed later).

The oscillatory flow rate in Fig. 6(a) reflects local variances of the slopes of individual levels, as seen in the corresponding level-dynamics picture on the left-hand side of Fig. 5(c). A deeper insight into the origin of the flow-rate oscillations can be gained in Fig. 7. This figure shows what we call a *Peres lattice* – according to Ref. [20], where this kind of visualization was introduced – constructed for

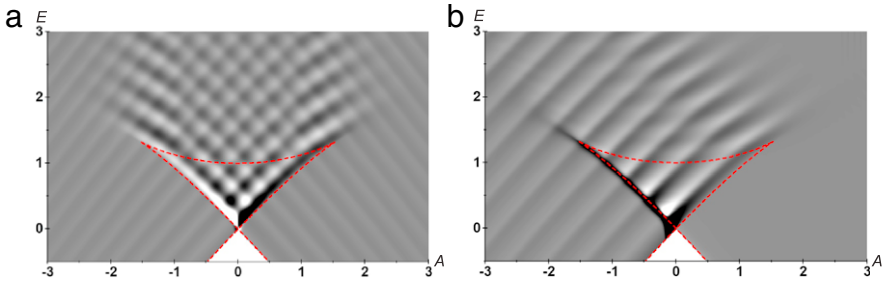

Fig. 6. The oscillatory component $\widetilde{\phi}^{\lambda}_{\sigma}(E)$ of the flow rate (Eq. (5)) for the CW Hamiltonian with parameter set #7 (panel a) and #4 (panel b). Bright (dark) tones indicate positive (negative) values, the dashed curves mark stationary points. Size and smoothing parameters: (a) $\aleph = 20, \sigma = 0.1$, (b) $\aleph = 20, \sigma = 0.08$.

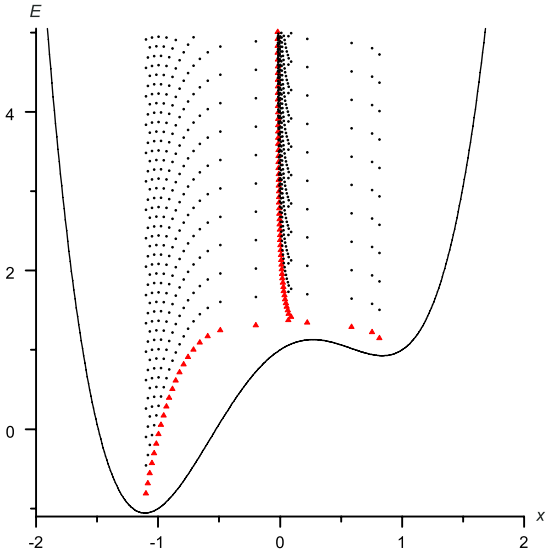

Fig. 7. (Color online) Peres lattice of quantum averages $\langle x\rangle^{\lambda}_i \equiv \langle\psi^{\lambda}_i|\frac{d}{d\lambda}\hat{H}^{\lambda}|\psi^{\lambda}_i\rangle$ versus $E^{\lambda}_i \equiv \langle\psi^{\lambda}_i|\hat{H}^{\lambda}|\psi^{\lambda}_i\rangle$ in individual energy eigenstates $|\psi^{\lambda}_i\rangle$ for the integrable CW Hamiltonian (17) with parameter set #7 at $A = 1$. The size parameter is $\aleph = 25$. The form of the corresponding double-well cusp potential is drawn. A sublattice of the eigenstates with $n_y = 0$ is marked by triangles.

the separable CW Hamiltonian with parameters as in the previous figure at $A = 1$. The points in this lattice depict averages $\langle P\rangle^{\lambda}_i \equiv \langle\psi^{\lambda}_i|\hat{P}|\psi^{\lambda}_i\rangle$ of a selected quantum observable $\hat{P}$ drawn against energies E^{λ}_i for individual Hamiltonian eigenstates $|\psi_i\rangle$. In the present case, the Peres observable $\hat{P}$ is identified with coordinate $\hat{x}$; the lattice therefore shows average locations of individual eigenstates with energy E^{λ}_i within the double-well potential. At the same time, since $\hat{x} = \frac{d}{d\lambda}\hat{H}^{\lambda}$, see Eq. (14), the application of the Hellmann–Feynman formula (6) leads to the identification of the coordinate average $\langle x\rangle^{\lambda}_i$ with the local slope $\frac{d}{d\lambda}E^{\lambda}_i$ of the corresponding energy level with respect to varying parameter $A \equiv \lambda$. In particular, the eigenstates located in the $x < 0$ minimum are descending together with this minimum ($\frac{d}{d\lambda}E^{\lambda}_i < 0$), and vice versa, the eigenstates located in the $x > 0$ minimum are ascending ($\frac{d}{d\lambda}E^{\lambda}_i > 0$). The horizontal spread of points contained within a certain energy bin of the Peres lattice therefore carries immediate information on the distribution of slopes in the selected portion of the spectrum. In this way, oscillations of the flow rate in Fig. 6(a) (at $A = 1$) can be directly related to the structures observed in the associated Peres lattice of Fig. 7.

We notice that the Peres lattice in Fig. 7 is rather regular—its points form a perfectly ordered pattern. This reflects integrability of the system. Taking into account separability of the Hamiltonian, one can generate the entire lattice from a basic sublattice corresponding to the $n_y = 0$ eigenstates (i.e., states formed by an arbitrary cusp eigenstate in combination with the oscillator ground state). It is clear that an infinite replication of this basic sublattice (in Fig. 7 shown by triangles) with a relative vertical shift $\Delta E = \hbar\Omega_y$ creates the lattice of all (n_x, n_y) eigenstates.

Based on the above observations, one can formulate the following conclusions of the present section: (i) Distinct finite-size precursors of an ESQPT in a separable system can be observed in oscillatory components of the state density and flow rate if the absolute rigidities (dynamical time scales) of both separated degrees of freedom differ substantially. (ii) These ESQPT precursors are "enhanced" in comparison with a generic 2D situation because they result from criticality of a 1D subsystem (in our case, the one connected with the x degree of freedom). (iii) If the 1D subsystem that exhibits criticality has the smaller rigidity (slower dynamics), one observes multiple replicas of the same set of ESQPT precursors. Each of these replicas is "well developed" since the effective 1D size parameter ($\aleph_x$ in our case) is relatively large. (iv) If the critical 1D subsystem has the larger rigidity (faster dynamics), one observes a single set of ESQPT precursors. They are "less developed" because the corresponding 1D size parameter is relatively small.

Let us stress that all these items remain valid for a general separable Hamiltonian of the simple form (20). One may anticipate that similar conclusions would be reproduced – at least to a certain extent – also for more general separable Hamiltonians of the form (19). Then, however, the (n_x, n_y) selection rules and the presence of ESQPT in effective 1D Hamiltonians $H[\hat{p}, \hat{x}, g(n_y)]$ with different values of n_y need to be analyzed case by case.

5. Chaotic dynamics

In the previous section, we have described and exemplified ESQPT precursors in the spectra of 2D separable systems which come as remnants of 1D ESQPT effects. Now we investigate what happens with these "*oscillatory structures*" (as we abbreviate all such effects) if the separability of the Hamiltonian is violated. While Section 5.1 merely collects basic observations, Section 5.2 attempts to record some relevant theoretical considerations.

5.1. Observations

The oscillatory component of the state density for non-separable, hence partially chaotic CW Hamiltonians with parameter sets from #1 to #4 is presented in Fig. 8. These results will be compared with Fig. 5, showing related dependences for separable, hence perfectly regular Hamiltonians. The comparison is pertinent because the selected separable and non-separable Hamiltonians yield the same values of the relative rigidity R^0 from Eq. (16). In particular, parameter set #1 (Fig. 8(a)) is related to the separable y-soft Hamiltonian with parameter set #5 (Fig. 5(a)), while parameter sets #2 and #3 (Fig. 8(b) and (c), respectively) are linked to the separable y-rigid Hamiltonian with parameter set #7 (Fig. 5(c)). Parameter set #4 (Fig. 8(d)) represents an asymmetric case, which has no analogy in the separable model. Table 1 summarizes the relevant features and parameters.

Quite surprisingly, Figs. 5 and 8 show a great deal of similarity. In particular, the oscillatory structures for both separable and non-separable y-soft Hamiltonians, depicted in Figs. 5(a) and 8(a), respectively, are nearly identical. Also the oscillatory structures associated with separable and non-separable y-rigid Hamiltonians, as seen in Fig. 5(c) and Fig. 8(b), (c), are similar, although in these cases the structures are conserved for non-separable Hamiltonians only in some fragments of the $\lambda \times E$ plane (note, in particular, the "checkered" pattern below and above the saddle point of the potential). The results for the asymmetric Hamiltonian in Fig. 8(d) have no integrable counterpart, but one again notices that the oscillatory structures exist only in a part of the $\lambda \times E$ plane. The oscillatory flow rate $\widetilde{\phi}^{\lambda}(E)$ associated with the same asymmetric Hamiltonian was depicted in Fig. 6(b), which confirms the above-discussed correlation with the oscillatory state density.

Fig. 9 presents another look at the oscillatory structures in the state density for parameter sets from #2 to #4. The parameters are the same as in panels (b)–(d) of Fig. 8, but the $\lambda \times E$ dependence of

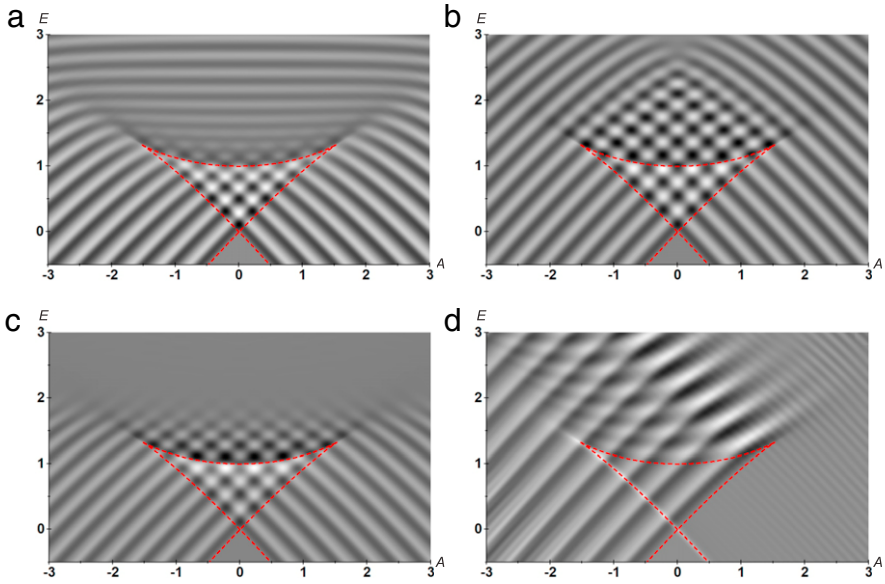

Fig. 8. Oscillatory state density $\widetilde{\rho}^{\lambda}_{\sigma}(E)$ for partially chaotic CW Hamiltonians with parameter sets #1 (panel a), #2 (panel b), #3 (panel c), and #4 (panel d) (cf. Fig. 2). Bright (dark) tones indicate positive (negative) values of $\widetilde{\rho}^{\lambda}_{\sigma}(E)$, dashed curves mark stationary points. Size and smoothing parameters: (a) $\aleph = 20/3$, $\sigma = 0.08$, (b) $\aleph = 20$, $\sigma = 0.1$, (c) $\aleph = 20$, $\sigma = 0.09$, (d) $\aleph = 20$, $\sigma = 0.08$.

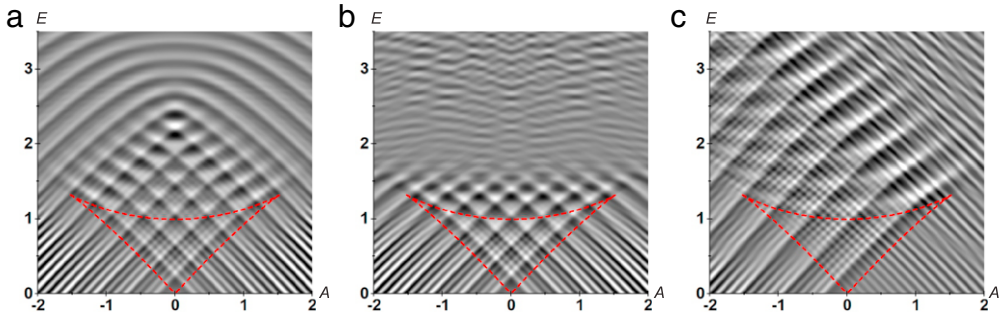

Fig. 9. Oscillatory state density $\widetilde{\rho}^{\lambda}_{\sigma}(E)$ for the CW Hamiltonians with parameter sets #2 (panel a), #3 (panel b), and #4 (panel c). The parameters are the same as in respective panels (b), (c), and (d) of Fig. 8, but the smoothing parameter is about twice smaller: $\sigma = 0.04$.

$\widetilde{\rho}$ is calculated with a smaller value of the smoothing parameter σ. The new plots display some tinier details of the state-density oscillations, which will be addressed in the forthcoming discussions. (Note that also the span of axes is taken differently than in Fig. 8.) From bird's perspective, the related panels in Figs. 8 and 9 show different views of the same landscape, where the separability-like structures play the dominant role. These structures thus represent robust effects, essentially independent of a particular choice of the smoothing parameter.

Parameter sets employed in the above calculations – see panels (a)–(d) of Fig. 8 – are the same as the parameter sets taken in the respective panel of Fig. 2, where we determined the fraction of regular dynamics f_{reg} in the $\lambda \times E$ plane for the corresponding Hamiltonians. At the first sight, the fragments of the oscillatory structures present in Fig. 8 appear to be correlated with the domains of increased regularity in Fig. 2. This is seen in panels (c) and (d) of Fig. 8, where the domains with nearly vanishing $f^{\lambda}_{\mathrm{reg}}(E)$ are virtually free of any oscillatory structures. However, a more careful inspection of

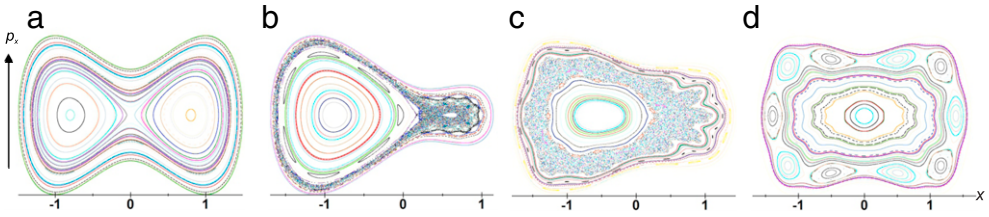

Fig. 10. (Color online) Selected Poincaré maps (composed of 10^5 passages of 50 trajectories through the $y = 0$ line) of the CW Hamiltonian with parameter set #2. Parameter A and energy E are: (a) $A = 0$, $E = 1.5$, (b) $A = 1.2$, $E = 1.5$, (c) $A = 1.2$, $E = 3$, (d) $A = 0$, $E = 3$.

these figures discloses that the correlation is only partial. In particular, the oscillatory structures exist even in the domains of very low values of the regular fraction. This is true for panel (a) of Fig. 8, which – in spite of considerably reduced regularity – is practically indistinguishable from the associated integrable case, and also for panel (d), where strong oscillatory structures protrude far into the highly chaotic region.

These findings can be further refined by a comparison of the oscillatory state density of the asymmetric Hamiltonian (parameter set #4) with Fig. 3, which presented Poincaré maps of the phase space for the same Hamiltonian. As we see, only a very small residue of a regular island in the Poincaré map suffices to generate a rather strong oscillatory structures in Figs. 8(d) and 9(c). This is particularly apparent in the Poincaré maps for $A = -2, -1$ at energy $E = 3$ and $A = 0, +1$ at $E = 1.5$: while the regular islands in these maps form only a marginal part of the phase space, the oscillatory structures in the relevant $\lambda \times E$ domains are still perfectly pronounced. The same conclusion applies also to the oscillatory flow rate in Fig. 6(b).

Four additional Poincaré maps belonging to the non-separable y-rigid Hamiltonian with parameter set #2 are depicted in Fig. 10. The displayed maps for $(A, E) = (0, 1.5), (1.2, 1.5), (1.2, 3)$ and $(0, 3)$ exhibit fully or partly regular dynamics and we see in Figs. 8(b) and 9(a) that the oscillatory structures are nicely developed at the corresponding places. However, the forms of these oscillatory structures in some cases differ from those in the associated integrable systems. Interpretation of these variations in terms of some details of the system's dynamics will be outlined below.

5.2. Discussions

Let us emphasize that the link between classical dynamics (Poincaré maps, classical orbits, regular fraction etc.) and here-studied type of quantum oscillatory structures is imperfect because the finite-size effects, by their nature, are not semiclassical. Nevertheless, there is no doubt that classical modes of motions present at given energy largely influence corresponding quantum properties of the system.

To understand the role of classical regularity in the formation of the ESQPT-related oscillatory structures, let us have a closer look at the forms of regular patterns in the associated Poincaré maps. For an exactly separable system with Hamiltonian (20), these patterns have specific shapes following from separate conservation of both partial Hamiltonians $H_x(p_x, x)$ and $H_y(p_y, y)$. In particular, the passages of any selected trajectory with energy E through the $y = y_0$ Poincaré section must lie on a curve given by $H_x(p_x, x) = E_x$, with a certain $E_x \in [E_0, E]$. Complementarily, passages of the same trajectory through the $x = x_0$ section would lie on a curve satisfying $H_y(p_y, y) = E_y$ with $E_y = E - E_x$. This means that the patterns formed in a given Poincaré map at energy E follow the shapes of trajectories in the associated direction for energies $\leq E$.

A general non-separable system can exhibit an *effective separability* in a limited part of the phase space. This means that the corresponding classes of trajectories consist of independent motions in x and y directions as if they were governed by a separable potential. One can think of a kind of an effective separable potential, which acts in a limited phase-space domain and has only a loose relation to the real potential $V^{\lambda}(x, y)$ of the system. Specifically, if the quasi-separable trajectory is y-rigid (i.e., if y motions are much faster than x motions), a natural way to derive an approximate

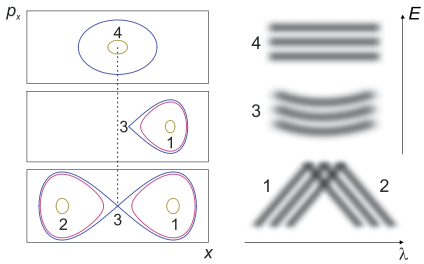

Fig. 11. Schematic view of various types of regular patterns (separable orbits in the CW potential) in the $y = 0$ Poincaré map (left) and their link to the associated oscillatory structures in the state density (right). The types of orbits: 1, 2—vibrations in the $x > 0$ and $x < 0$ potential wells, 3—orbits containing a singular point with asymptotic crossing time, 4—stabilized vibrations above the saddle of the potential.

effective potential governing the dynamics in the x direction leads via replacing y^2 and p_y^2 in the CW Hamiltonian (14) by the respective time averages $\langle y^2\rangle$ and $\langle p_y^2\rangle$. This yields:

$$V_{\mathrm{eff}}^{\lambda}(x) \approx x^4 + \underbrace{\left(A + B\langle y^2\rangle\right)}_{a} x + \underbrace{\left(-2 + C\langle y^2\rangle\right)}_{b} x^2 + \underbrace{1 + \frac{\langle p_y^2\rangle}{2} + D\langle y^2\rangle}_{c=E_y+\mathrm{const}} \equiv V_{\mathrm{cusp}}(x). \tag{28}$$

We identify this expression with the cusp potential, the shape parameters a and b depending on the CW parameters A, B, C and on $\langle y^2\rangle$. Note that c can be written as a sum of energy component E_y and an arbitrary additive constant.

The effective potential in Eq. (28) helps to understand the examples of partially separable y-rigid motions analyzed here. In particular, it follows that the increase of $\langle y^2\rangle$ (that takes place when one ascends the oscillatory structures with growing energy E_y) leads to an increase of cusp parameters a (for $B > 0$) and/or b. This causes an effective shift of parameter A and lowering or disappearance of the double-well shape of the effective potential. Both these phenomena indeed affect the oscillatory structures with increasing energy in Figs. 8 and 9. However, one should not forget that Eq. (28) is only an approximation.

Below, we outline a basic typology of quasi-separable motions that we actually observe in the present model. A schematic picture of related patterns in Poincaré maps and their link to the corresponding oscillatory structures in the state density are given in Fig. 11. Numbers 1 and 2 in this figure correspond to low-amplitude vibrations around both potential minima. These motions naturally satisfy the separability condition due to the harmonic approximation. Regular patterns (ellipses) created by such trajectories are present in Poincaré maps of Figs. 3 and 10(a)–(c). Away from the critical point ($A \neq 0$) and for asymmetric potentials ($B \neq 0$), regular vibrations are not equally developed in both wells and in some cases they appear only in one of them. An associated oscillatory structure in the state density appears above the respective minimum and a similar effect is generated in the flow rate—cf. Figs. 6, 8 and 9. It turns out that these oscillatory structures are present even if the corresponding regular islands in the Poincaré map are very small.

For sufficiently high energies, stabilized vibrations can occur also above the saddle of the CW potential, thus in a seemingly unstable domain. These are the orbits of type 4 in the upper-left part of Fig. 11, documented by real specimens in Fig. 10(d). In the y-rigid case, the vibrations of this peculiar kind can be related to the $x = 0$ minimum of the effective cusp potential (28) with $b > 0$, which applies if $C\langle y^2\rangle > 2$. These motions are responsible for the state-density oscillatory structure sketched under no. 4 in Fig. 11-right. Such horizontal strips are indeed observed in the uppermost part of Fig. 9(a).

Oscillatory structures of type 3 on the right in Fig. 11, i.e., the shifted replicas of the $\smile$ shaped "caps" of the ∇ profile, which are well distinguished in Fig. 9(a), (c), result from some singular orbits that in the $y = 0$ Poincaré map produce regular patterns with a sharp vertex at a certain $x = x_0$ and $p_x = 0$ (see the patterns no. 3 in Fig. 11-left). In the y-rigid case, the x component of these orbits can be derived from Eq. (28), with the total energy E equal to the height of the potential barrier separating

both minima of the effective cusp potential. The vertex in the Poincaré map represents an asymptotic point of the trajectory, located at the barrier top, which is unreachable in a finite time. For a fully symmetric system, the pattern of type 3 appears on both sides of the barrier, as sketched in bottom-left part of Fig. 11 and exemplified in Fig. 10(a). However, similar orbits can occur also with only a single lobe (see middle-left scheme of Fig. 11), the other part being destroyed by chaos—examples seen in Figs. 3 and 10(b). It should be clarified that the vertex is not in general located at the saddle point $x^{\lambda}_{\mathrm{sad}}$ of the actual CW potential, but rather follows the maximum of the effective cusp potential (28). The use of $V^{\lambda}_{\mathrm{eff}}(x)$ instead of $V^{\lambda}(x, y)$ explains the observed systematic shifts of the "cap" structures in Fig. 9(c) to lower values of parameter A.

To complement the above classical considerations, we turn at last to the discussion of quantum Peres lattices. These represent a quantum analog of classical Poincaré maps—instead of regular/chaotic trajectories they visualize regular/chaotic eigenstates of the quantum Hamiltonian (points located in ordered/disordered parts of the lattice) [21]. Several Peres lattices associated with the partially chaotic parameter sets of the CW Hamiltonian are shown in Fig. 12. The concord with classical chaos is illustrated by the lattice in panel (a) in conjunction with the associated regular fraction in panel (b). Two additional Peres lattices for the same parameter set #4 (cf. Fig. 2(d)) but different values of A (given in each panel) are depicted in column (c) of Fig. 12. Together, the three lattices visualize a process of gradual disappearance of the regular part of spectrum, which is associated with eigenstates located in the more regular potential well at $x > 0$. As this well rises with increasing $A \equiv \lambda$, the irregular part of spectrum (associated with the descending chaotic well at $x < 0$) collects an increasing number of states. A related process for other parameter choices is sketched in the rest of Fig. 12—column (d) shows two Peres lattices for parameter set #2 (cf. Fig. 2(b)), column (e) presents lattices for parameter set #3 (cf. Fig. 2(c)).

All together, the Peres lattices in Fig. 12 can be compared with the oscillatory structures in Figs. 8(b)–(d) and 9(a)–(c). In particular, we observe that oscillatory structures above the $x < 0$ or $x > 0$ minimum of the CW potential appear if an ordered sublattice exists in the respective potential well. Note that the ordered sublattice usually significantly exceeds above the upper energy edge of the well. This is in agreement with the regular patterns present in the classical Poincaré maps. On the other hand, if the sublattice belonging to a given potential well is mostly disordered, the associated oscillatory structure is absent.

Besides the $\langle x\rangle < 0$ and $\langle x\rangle > 0$ sublattices, the Peres lattices in Fig. 12 contain also a surprisingly large subset of states that dwell above the saddle of the potential, in a relatively narrow coordinate interval near $\langle x\rangle \sim 0$. As we know, these states can also have their regular counterparts in Poincaré maps and may generate specific oscillatory structures. Although for states of this kind, the distinction between order and disordered sublattices is less obvious than before, we can unambiguously decide that the $\langle x\rangle \sim 0$ sublattice in column (d) of Fig. 12 is certainly more ordered than the corresponding portion of the lattice in column (e). This is in accord with the occurrence of oscillatory structures and with the classical analysis.

The link of the above-studied Peres lattices to flow properties of the CW spectrum is demonstrated in Fig. 13. It shows constrained level dynamics of the asymmetric Hamiltonian with parameter set #4. The lines in this figure (corresponding to individual level energies E^{λ}_i) are sorted according to the local slope $\frac{d}{d\lambda}E^{\lambda}_i$ so that the lines with positive slopes appear in panel (a), those with nearly vanishing slopes in panel (b), and lines with negative slopes in panel (c). In view of the Hellmann–Feynman formula (6), these three panels collect levels whose wave functions are centered in various coordinate domains: (a) in the rising, more regular potential well at $x > 0$, (b) in the chaotic (for this parameter set) region around $x \sim 0$, and (c) in the descending, prevailingly chaotic well at $x > 0$. This visualization is consistent with the Peres lattices in Fig. 12 and can be directly compared with the corresponding oscillatory state density in Figs. 8(d) and 9(c), and with the oscillatory flow rate in Fig. 6(b). In particular, we notice in Fig. 13(a) a separability-induced structure for states located in the regular potential minimum.

Based on these findings, we formulate the following conclusions concerning ESQPT finite-size precursors in the spectra of non-integrable CW Hamiltonians: (i) The separability-induced oscillatory structures in the state density are conserved to a surprisingly high extent also for non-separable Hamiltonians. (ii) The oscillatory structures invariantly appear in all partly regular domains of the

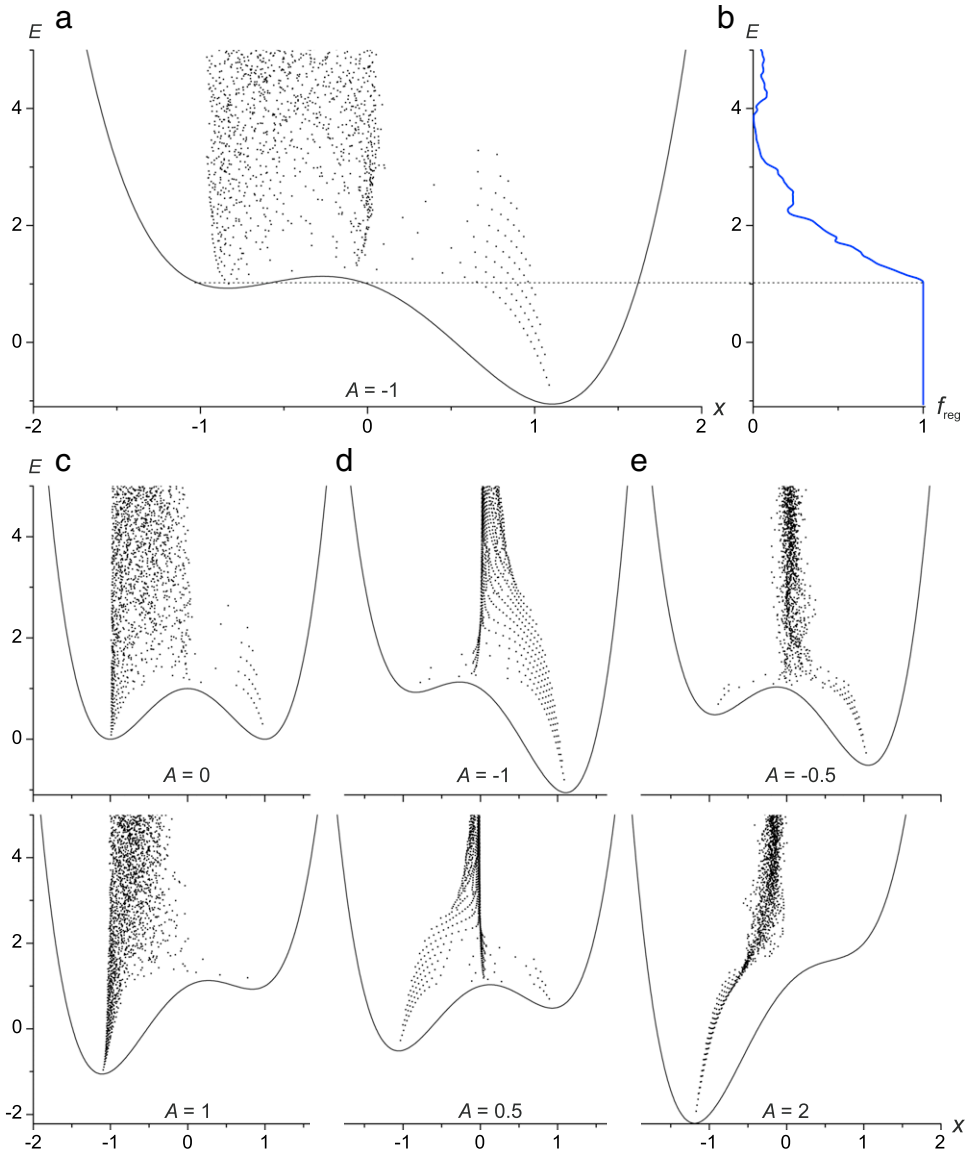

Fig. 12. Peres lattices for observable $\hat{P} = \hat{x}$ (its average is on the horizontal axis) for the CW Hamiltonian with several parameter choices: Panel (a) and column (c) show three lattices for parameter set #4, column (d) depicts two lattices for parameter set #2, and column (e) two lattices for parameter set #3. In all cases we take $\aleph = 25$. The $y = 0$ cut of the corresponding potential is indicated in each lattice. Panel (b) shows the regular fraction corresponding to panel (a); the horizontal line marks occurrence of first chaotic states.

plane $\lambda \times E$, even those with relatively small values of the regular fraction. It seems that within the CW model, the increase of regularity is generally connected with emergence of a partial, effective separability of dynamics, which supports the occurrence of oscillatory structures. (iii) The type of the oscillatory structure observed in the spectrum depends on the type of underlying dynamics. We have developed a typology of classical orbits responsible for various kinds of oscillatory structures, see Fig. 11. (iv) Peres lattices provide a complementary view of the regularity-related effects. With

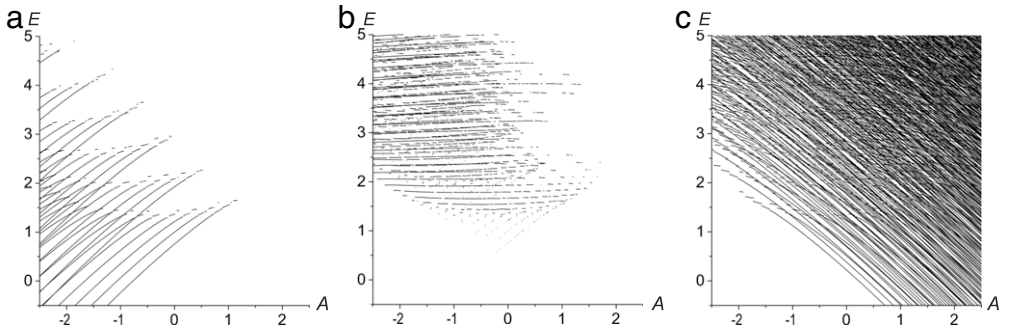

Fig. 13. Constrained level dynamics of the CW Hamiltonian with parameter set #4 for $\aleph = 10$, separated into three components according to slopes of levels with variable $\lambda \equiv A$: (a) the rising (regular) part of the spectrum with $+0.1 < \frac{d}{d\lambda} E_i^{\lambda}$, (b) about horizontal part, $-0.1 < \frac{d}{d\lambda} E_i^{\lambda} < +0.1$, and (d) the descending (chaotic) part, $\frac{d}{d\lambda} E_i^{\lambda} < -0.1$.

a proper choice of the Peres operator, they substantially help to visualize level dynamics and flow properties of the spectrum.

6. Summary and outlook

This work continues our systematic study of excited-state quantum phase transitions in systems with a few (particularly two) degrees of freedom f. In part I [1], we described the ESQPT defining properties in terms of non-analytic dependences of the smooth component of the quantum state density on the control parameter λ and energy E. We explained that for "finite systems" (whose f remains finite even for infinite size parameter $\aleph$), these properties are based purely on the classical limit. Non-analyticities in the $\aleph \to \infty$ spectrum, which affect smooth components of the state density and spectral flow, as well as the related thermodynamical quantities, are derived from stationary points of the classical Hamiltonian.

In the present part II, our attention has been focused on the oscillatory components of the state density and flow rate in a vicinity of an ESQPT. These quantities describe spectral fluctuations in the $\lambda \times E$ plane, namely the clustering of energy levels in a λ-fixed spectrum and laminarity or turbulence of the flow of levels with varying λ. Although the oscillatory components represent just finite-size effects (in the $\aleph \to \infty$ limit they are washed out by an arbitrary $\sigma \to 0$ smoothing procedure), we have demonstrated that they can constitute important ESQPT precursors, which in some cases even prevail the defining properties in terms of the smooth components.

As in part I, we have studied here the ESQPT structures accompanying the first-order ground-state QPT in a generalized Creagh–Whelan model. The potential of this $f = 2$ model bears similarities to the $f = 1$ cusp model in coordinate x, but the y degree of freedom obviously leads to significant modifications. Nevertheless, in some cases the 1D ESQPT structure of the underlying cusp potential remains largely present in finite-size spectra of the full $f = 2$ model. This is connected with a partial effective separation of the x and y modes of motions, hence with a partly increased degree of regularity of the corresponding CW Hamiltonian.

The 1D ESQPT structures in finite-size spectra are most apparent if the time scales of both partially separated modes (thus the effective size parameters $\aleph_x$ and $\aleph_y$) are highly imbalanced. In this situation, the state-density oscillations due to the soft mode can be averaged out by an appropriate smoothing procedure, which at the same time preserves the state-density oscillations caused by the rigid mode. The ESQPT precursors are particularly enhanced relative to a generic $f = 2$ case if $\aleph_x$ (size parameter of the critical subsystem) is much larger than $\aleph_y$. Then the 1D ESQPT structures in the spectrum of the whole system are more developed and come in multiple replicas.

It has been shown in the numerical part of our analysis that the 1D ESQPT structures are strongly resistant to the rise of chaos in the system. Surprisingly, even a very small regular island – domain in the phase space where trajectories are governed by an effectively separable Hamiltonian – generates

quite large oscillatory structures in the spectrum. We anticipate that similar effects exist in a broad class of $f = 2$ systems and that they will soon become available experimentally.

In the intended part III of this series, we will explore the general findings of parts I and II in the setting of genuine interacting many-body systems, where effects of more involved kinetic terms beyond $\vec{p}^{\,2}/2$ are important.

Acknowledgments

This work was performed under the project no. P203-13-07117S of the Czech Science Foundation. P.S. acknowledges support by CONACyT and PAPIIT-UNAM, Mexico. A.L. and M.M. appreciate the funding by Israel Science Foundation and the Golda Meir Fellowship.

Appendix. Periodic orbit approximation in 2D separable systems

The aim of this appendix is to show that the last term of expression (23) for the oscillatory component $\widetilde{\rho}^{\lambda}(E)$ of the total state density of a *separable system* with $f = 2$ allows one to derive the periodic-orbit approximation (11) in dimension 2. We start by expressing both 1D oscillatory components $\widetilde{\rho}_*(E_*)$ of the $* = x, y$ state densities in the form of Eq. (11):

$$\widetilde{\rho}_*(E_*) \approx \frac{T_*(E_*)}{\pi\hbar}\sum_{r_*=1}^{\infty}\cos\left[\frac{r_* I_*(E_*)}{\hbar} - r_*\phi_*\right] = \frac{T_*(E_*)}{2\pi\hbar}\sum_{k_*=\pm1}^{\pm\infty} e^{ik_*\left[\frac{I_*(E_*)}{\hbar}-\phi_*\right]}. \tag{A.1}$$

As shown in Ref. [22], this formula jointly with the $r_* = 0$ term, which represents the smooth component $\bar{\rho}_*(E_*) = T_*(E_*)/\pi\hbar$ of the state density [1], exactly reproduces the spectrum obtained from the semiclassical quantization. The function $I_*(E_*)$ is the action over the *primitive* (nonrepeated) periodic orbit, $T_*(E_*) = \frac{\partial}{\partial E_*} I_*(E_*)$ is the corresponding period, and ϕ_* stands for a constant phase factor related to the Maslow index of the orbit [10,11]. For simplicity, we assume here a single-well 1D potential, for which there exists just one primitive orbit at any E_*. The integer $|k_*| \equiv r_*$ counts the number of loops completed around the given primitive orbit.

Evaluating the last term in Eq. (23), i.e., the convolution of the x and y oscillatory components, one obtains:

$$\widetilde{\rho}(E) \approx \frac{1}{(2\pi\hbar)^2}\sum_{k_x=\pm1}^{\pm\infty}\sum_{k_y=\pm1}^{\pm\infty}\int T_x(E_x)T_y(E-E_x)e^{i\left[\frac{k_x I_x(E_x)+k_y I_y(E-E_x)}{\hbar}-(k_x\phi_x+k_y\phi_y)\right]}dE_x. \tag{A.2}$$

For a 2D separable system, the expression of the classical Hamiltonian in action variables reads as $H = H_x(I_x) + H_y(I_y)$. We therefore proceed via the substitution $E_x \mapsto I_x$, with $E_x = H_x(I_x)$ and $dE_x/dI_x = 1/T_x$. In view of the oscillating character of the subintegral function in Eq. (A.2), the use is made of the stationary phase approximation, which in 1D reads as: $\int g(x)e^{if(x)}dx \approx \sqrt{2\pi/|f''(x_0)|}g(x_0)e^{if(x_0)}e^{i\pi\,\mathrm{sgn}f''(x_0)/4}$, with x_0 denoting a stationary point of $f(x)$. In the present case, the stationary-phase condition is written as $k_x + k_y(dI_y/dE_y)(-dH_x/dI_x)$, which yields:

$$k_x T_x = k_y T_y. \tag{A.3}$$

This means that the ratio $\mathcal{R}(E, I_x) \equiv T_y(E - H_x(I_x))/T_x(I_x)$ of the periods corresponding to x- and y-motions takes a rational value $k_x/k_y > 0$ at the stationary point $I_x = I_x^0(E)$. We can write: $\vec{k} \equiv (k_x, k_y) = (r\mu_x, r\mu_y) \equiv r\vec{\mu}$, where $\mu_x > 0$ and $\mu_y > 0$ are two incommensurable integers and $r = \pm1, \pm2, \ldots$. Condition (A.3) then identifies a primitive periodic orbit $o(\vec{\mu})$ with period $T_{o(\vec{\mu})} = \mu_x T_x = \mu_y T_y$ repeated $|r|$ times. Due to separability of the Hamiltonian, the action of the primitive orbit is: $I_{o(\vec{\mu})} = \mu_x I_x + \mu_y I_y$. The denominator $f''(x_0)$ in the stationary-phase expression reads as $\frac{\partial}{\partial I_x}\mathcal{R}(E, I_x)|_{I_x^0} \equiv \mathcal{R}'_{o(\vec{\mu})}$ and its sign is $r/|r|$. Putting all these findings together, we obtain the following formula:

$$\widetilde{\rho}(E) \approx \frac{1}{2\pi\hbar}\sum_{\vec{\mu}}\sum_{r=\pm1}^{\pm\infty}\frac{T_{o(\vec{\mu})}(E)}{\sqrt{2\pi\hbar(r\mu_y)^3|\mathcal{R}'_{o(\vec{\mu})}(E)|}}e^{ir\left[\frac{I_{o(\vec{\mu})}}{\hbar}-(\mu_x\phi_x+\mu_y\phi_y)+\frac{\pi}{4|r|}\right]}. \tag{A.4}$$

At last, joining the $+r$ and $-r$ terms of Eq. (A.4) and identifying $r(\mu_x\phi_x + \mu_y\phi_y) + \pi/4$ with $\phi_{\mathrm{ro}(\vec{\mu})}$, we arrive at an expression of the desired general form (11).

It needs to be stressed that Eq. (A.4) does not contain quasi-1D orbits generated by periodic motions only in x- or y-direction, i.e., the orbits having either $\mu_x = 0$ or $\mu_y = 0$. Such orbits play an important role in the creation of the oscillatory structures studied in this work. However, being contained only in the cross-terms of Eq. (23), these orbits yield vanishing contribution in the stationary phase approximation.

References

[1] P. Stránský, M. Macek, P. Cejnar, Ann. Phys. (NY) 345 (2014) 73.
[2] P. Cejnar, M. Macek, S. Heinze, J. Jolie, J. Dobeš, J. Phys. A 39 (2006) L515.
[3] M.A. Caprio, P. Cejnar, F. Iachello, Ann. Phys. (NY) 323 (2008) 1106.
[4] P. Cejnar, P. Stránský, Phys. Rev. E 78 (2008) 031130.
[5] D. Larese, Pérez-Bernal, F. Iachello, J. Mol. Struct. 1051 (2013) 310.
[6] B. Dietz, F. Iachello, M. Miski-Oglu, N. Pietralla, A. Richter, L. von Smekal, J. Wambach, Phys. Rev. B 88 (2013) 104101.
[7] T. Brandes, Phys. Rev. E 88 (2013) 032133.
[8] M.A. Bastarrachea-Magnani, S. Lerma-Hernández, J.G. Hirsch, Phys. Rev. A 89 (2014) 032101;
M.A. Bastarrachea-Magnani, S. Lerma-Hernández, J.G. Hirsch, Phys. Rev. A 89 (2014) 032102.
[9] M. Kastner, Rev. Modern Phys. 80 (2008) 167.
[10] F. Haake, Quantum Signatures of Chaos, Springer-Verlag, Berlin, 1991.
[11] H.-J. Stöckmann, Quantum Chaos: An Introduction, Cambridge University Press, Cambridge, UK, 1999.
[12] M.C. Gutzwiller, J. Math. Phys. 12 (1971) 343.
[13] M.V. Berry, M. Tabor, Proc. R. Soc. Lond. Ser. A 349 (1976) 101. A 356 (1977) 375.
[14] V.I. Arnold, Mathematical Methods of Classical Mechanics, Springer-Verlag, Berlin, 1989.
[15] S.C. Creagh, N.D. Whelan, Ann. Phys. (NY) 272 (1999) 196.
[16] P. Cejnar, P. Stránský, AIP Conf. Proc. 1575 (2014) 23. See also arXiv:1410.3618 [nucl-th].
[17] P. Stránský, M. Kurian, P. Cejnar, Phys. Rev. C 74 (2006) 014306.
[18] I. Stewart, Rep. Progr. Phys. 45 (1982) 185.
[19] A large collection of results can be found on the website: http://www.pavelstransky.cz/cw.php.
[20] A. Peres, Phys. Rev. Lett. 53 (1984) 1711.
[21] P. Stránský, P. Hruška, P. Cejnar, Phys. Rev. E 79 (2009) 046202;
P. Stránský, P. Hruška, P. Cejnar, Phys. Rev. E 79 (2009) 066201.
[22] M. Berry, K.E. Mount, Rep. Progr. Phys. 35 (1972) 315.